



INSTITUTO DE FÍSICA

Universidade Federal Fluminense

**PHOTOCATALYTIC WATER RADIOLYSIS USING SEMICONDUCTOR MATERIALS:
ENHANCING EFFICIENCY FOR SUSTAINABLE HYDROGEN PRODUCTION**

Thiago Rocha Girão Souza

Advisor: Prof. Dr. Lucas Mauricio Sigaud

UFF - Universidade Federal Fluminense

Niterói, 2023

Universidade Federal Fluminense
Instituto de Física
Coordenação do Curso de Graduação em Física

**PHOTOCATALYTIC WATER RADIOLYSIS USING SEMICONDUCTOR MATERIALS:
ENHANCING EFFICIENCY FOR SUSTAINABLE HYDROGEN PRODUCTION**

Thiago Rocha Girão Souza

Thesis presented to the Graduate
Program in Physics at UFF as a partial
requirement for obtaining the degree
of Master in Physics.

Advisor: Prof. Dr. Lucas Mauricio Sigaud

Niterói
2023

Ficha catalográfica automática - SDC/BIF
Gerada com informações fornecidas pelo autor

S719p Souza, Thiago Rocha Girão
PHOTOCATALYTIC WATER RADIOLYSIS USING SEMICONDUCTOR
MATERIALS: ENHANCING EFFICIENCY FOR SUSTAINABLE HYDROGEN
PRODUCTION / Thiago Rocha Girão Souza. - 2023.
79 f.

Orientador: Lucas Mauricio Sigaud.
Dissertação (mestrado)-Universidade Federal Fluminense,
Instituto de Física, Niterói, 2023.

1. Física Atômica. 2. Radiólise Catalítica da Água. 3.
Radiação Ionizante. 4. Espectrometria de Massa. 5.
Produção intelectual. I. Sigaud, Lucas Mauricio, orientador.
II. Universidade Federal Fluminense. Instituto de Física.
III. Título.

CDD - XXX

Thiago Rocha Girão Souza

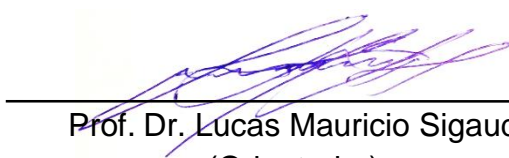
**PHOTOCATALYTIC WATER RADIOLYSIS USING SEMICONDUCTOR
MATERIALS: ENHANCING EFFICIENCY FOR SUSTAINABLE
HYDROGEN PRODUCTION**

Dissertação submetida ao curso de pós-graduação em Física da Universidade Federal Fluminense, como requisito parcial para obtenção do Título de Mestre em Física.


Aprovado em:31/08/2023.

BANCA AVALIADORA

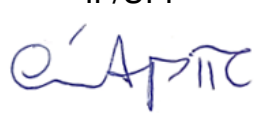
Membros titulares



Prof. Dr. Lucas Mauricio Sigaud
(Orientador)
IF/UFF



Prof. Dr. Pedro Paulo de Mello Venezuela
IF/UFF



Dra. Cíntia Aparecida Pires da Costa
ENSICAEN

Abstract

This thesis explores the potential of semiconductor photocatalysts in enhancing the efficiency of hydrogen production via water radiolysis. As the demand for sustainable and clean energy sources continues to rise, the use of hydrogen, particularly 'green' hydrogen produced through water radiolysis, is attracting increasing attention. The primary focus of this work is the experimental investigation of photocatalytic water radiolysis, with an emphasis on the role of semiconductor materials in this process.

The study employs an experimental setup designed to observe the products of water radiolysis, specifically monitoring the yield of molecular hydrogen. Experiments were conducted under various conditions using different proportions of photocatalysts. The experimental results confirmed the Honda-Fujishima effect, demonstrating an enhancement in H_2 production with the introduction of photocatalysts.

Furthermore, the thesis discusses the capability and suitability of the experimental apparatus and methodology used for the measurement of H_2 yields, confirming their effectiveness in capturing accurate and reliable data.

Key-Words: Atomic Physics, Ionizing Radiation, Photocatalytic Water Radiolysis, Mass Spectrometry.

Resumo

Nesta dissertação, investigamos o papel dos fotocatalisadores semicondutores na otimização da produção de hidrogênio através da radiólise da água. Com o crescente interesse por fontes de energia limpas e sustentáveis, o hidrogênio, em particular o ‘hidrogênio verde’ gerado por radiólise da água, tornou-se um foco de pesquisa relevante. Este trabalho é dedicado ao estudo experimental da radiólise da água com fotocatalise, dando destaque à atuação dos materiais semicondutores nesse procedimento.

Para alcançar nossos objetivos, utilizamos um aparato experimental desenvolvido para monitorar os produtos da radiólise da água, enfocando no rendimento do hidrogênio. Realizamos experimentos sob várias condições, empregando diferentes proporções de fotocatalisadores. Os resultados obtidos confirmaram o efeito Honda-Fujishima, demonstrando uma melhora na produção de H_2 com a introdução de fotocatalisadores.

Adicionalmente, esta dissertação discute a eficiência e a adequação do aparato e da metodologia experimental utilizados para a medição dos rendimentos de H_2 , ratificando sua efetividade na captação de dados confiáveis e precisos.

Palavras-chave: Física Atômica, Radiação Ionizante, Radiólise Fotocatalítica da Água, Espectrometria de Massa.

Table of Contents

1	INTRODUCTION	9
2	WATER RADIOLYSIS: UNVEILING ITS STAGES AND AM- PLIFYING H_2 GENERATION	12
2.1	Water radiolysis	13
2.1.1	Physical stage ($0 - 10^{-15}$ s)	14
2.1.2	Physico-chemical stage ($10^{-15} - 10^{-12}$ s)	19
2.1.3	Chemical stage ($10^{-12} - 10^{-6}$ s)	24
2.2	Photocatalytic water splitting	26
3	EXPERIMENTAL SETUP AND PROCEDURE	31
3.1	Irradiation chamber	31
3.2	Vacuum system	33
3.3	Radiation source	35
3.4	Semiconductor materials	37
3.5	Mass spectrometer (TOFMS)	40
4	RESULTS DISCUSSION AND IMPLICATIONS	45
4.1	Background measurement	45
4.2	Theoretical predictions of measured molecules	47
4.3	Post-irradiation experimental results	51
5	CONCLUSIONS AND FUTURE DIRECTIONS	56
	REFERENCES	59
A	WATER MOLECULE	62
A.1	Molecular structure	62

A.2	Molecular orbitals	64
A.3	Hydrogen bonding	67
	B GROUP THEORY	69
B.1	What is a Group?	69
B.2	Classification of groups	70
B.3	Group Representation	72
B.4	Transformation Groups	75
B.5	Characters of a representation	78

Chapter 1

Introduction

Water radiolysis, which refers to the irradiation of water by ionizing particles and the subsequent molecular fragmentation, is a well-known and studied phenomenon for approximately a century [1]. Nowadays, the investigation of water radiolysis and its products is associated with various applications in fields such as biology, cosmology, geophysics, and particularly in the sustainable development of the planet [2]. This serves as the primary motivation for conducting this research, guiding the modeling and construction of the experimental apparatus. Within this context, this study focuses on examining the mechanism responsible for the formation of molecular hydrogen during the radiolysis of liquid water.

Although hydrogen is the most abundant element in the universe [3], there is a challenge in the formation of H_2 due to the inefficient direct reaction between two hydrogen atoms colliding in the gaseous state. This stems from the requirement of rapidly releasing an excess energy of approximately 4.5 eV by the molecule, which is formed in a highly vibrational state, to achieve stability [4]. In the gaseous state, the molecule remains isolated, and the only way to attain the necessary energy release is through photon emission. However, such a transition is not permitted in this particular case according to dipole selection rules. The solution to this problem lies in a three-body reaction (with the third body carrying this excess energy). In the interstellar medium, for instance, due to the low densities involved, the third body cannot be another atom, not even H, but instead must be a cosmic dust grain [2].

Therefore, water radiolysis emerges as a clean method for obtaining H_2 , distinct from other sources that involve fossil fuels and hydrocarbons [5].

However, the process of water splitting into its constituent parts, such as hydrogen and oxygen, is an uphill reaction. That is a type of chemical reaction that requires energy input to proceed, with a positive Gibbs free energy change of $\Delta G = +238 \text{ kJ/mol}$, which means it is not thermodynamically favorable and the energy required can come from various sources, such as heat, light or an electrical potential difference. In practical terms, a positive ΔG means that the reaction is not spontaneous and that the reactants have a higher free energy than the products, and energy must be added to the system to convert the reactants into products [6].

Therefore, semiconductor materials, alongside radiation sources, can play an important role in water splitting through the process of photocatalysis. In this process, a semiconductor material, such as zirconium dioxide (ZrO_2), is irradiated with light in the presence of water, providing a promising method for producing hydrogen fuel from water using renewable energy sources. It has the potential to become a key technology for achieving a sustainable and carbon-free energy future [6].

There are still unresolved issues regarding the phenomena occurring during radiolysis in the liquid phase of water, which are primarily investigated through simulations. The purpose of this study is to investigate the production of H_2 and its optimization concerning the presence of semiconductor materials in liquid water.

In short, the experiment consists of a container containing liquid water with a quartz recess-like window where the radiation source will be placed. Since H_2 is volatile, once formed, it will quickly be ejected from the liquid medium and can be measured by coupling the experimental apparatus to a time-of-flight mass spectrometer (TOF). The presence of different semiconductor materials in an aqueous environment leads to different measurements of produced H_2 , and such data were appropriately compared. Furthermore, other factors that must be taken into consideration are the beam energy, system temperature, and irradiation time.

In addition to describing the aforementioned experimental apparatus, this study presents the measurement protocol employed, which demonstrates the feasibility and capability of producing and measuring H_2 through this process. The obtained results are consistent with the data found in the literature.

Chapter 2

Water radiolysis: unveiling its stages and amplifying H_2 generation

The interaction between ionizing radiation and water initiates a cascade of complex reactions, leading to the decomposition of water molecules into highly reactive species. These reactive species play a pivotal role in numerous chemical and biological processes, making this process known as water radiolysis a subject of great interest and scientific investigation [7].

Water radiolysis can be evaluated using both quantitative and qualitative approaches. Quantifying the yield of specific radiolysis products can be done through experimental measurements or Monte Carlo simulations, incorporating information on cross-sections, energy deposition and reaction rates [8]. This involves determining the concentration or amount of the product formed per unit of energy and it takes into account parameters such as radiation energy, radiation dose, and the presence of catalysts.

Comparing the outcomes of water radiolysis under different experimental conditions and examining differences in product yields can provide qualitative insights into the influence of these factors on water radiolysis.

Therefore, combining quantitative measurements and qualitative observations allows for a comprehensive evaluation of water radiolysis, providing a deeper understanding of the underlying processes and their implications in various applications.

Understanding the environment in which the mechanism of water radiolysis takes place is crucial for comprehending the intricacies of this fascinating phenomenon. To fully grasp the complex series of reactions and their outcomes, it is necessary to visualize the scenario in which water molecules are exposed to ionizing radiation.

2.1 Water radiolysis

Water radiolysis encompasses three overlapping stages: physical, physico-chemical and non-homogeneous chemical stages. In the initial stage, ionizing radiation interacts with water molecules, causing ionization and the formation of positively charged ions (H^+) and free electrons (e^-). This sets the stage for the subsequent dissociation stage, where further reactions occur, generating highly reactive species. Notably, the hydroxyl radical (OH) forms as electrons combine with water molecules, resulting in the detachment of hydrogen atoms. Additionally, hydrated electrons (e_{aq}^-) are produced as excess electrons become solvated by surrounding water molecules. In the final recombination stage, these reactive species engage in various reactions, leading to the production of molecular hydrogen (H_2) and other byproducts. The hydroxyl radical can react with itself or hydrogen atoms, while hydrated electrons partake in recombination reactions that generate H_2 [7].

In this context, there is a quantitative measure, known as G-value, typically expressed as the number of molecules or radiolysis species produced per 100 eV of absorbed energy. These formed products are diffused throughout the medium and can react with other water molecules, and these probabilities of reaction are in accordance with the equilibrium constants of chemical reactions, which, in turn, are well-known factors [9].

It is also important to highlight the presence of scavengers in the process. Scavengers are chemical species that readily react with and neutralize the highly reactive species generated during water radiolysis, such as the hydrated electrons, which, in turn, are the main precursor of H_2 [10].

It is possible to gain a qualitative understanding of the mechanism of water radiolysis

by temporally delineating each of its stages.

2.1.1 Physical stage ($0 - 10^{-15}$ s)

The first stage of water radiolysis is characterized by the primary ionization of water molecules when exposed to ionizing radiation. In this stage, we can estimate the number of ions formed by considering known parameters such as the cross-section of ionization on water and the number of scattering centers.

The cross-section of ionization on water (σ) represents the probability of ionization occurring per unit area of the target material, in this case, water. It quantifies the likelihood of a water molecule being ionized when interacting with the incident radiation.

The number of scattering centers is a measure of the total number of water molecules within the interaction region. It represents the number of water molecules per cm^3 (n) multiplied by the area of the radiation beam (A) and a certain length (Δx) along its path.

By multiplying the cross-sections of ionization on water by the number of scattering centers, we can estimate the number of ionizations occurring in the target material. This estimation provides insights into the initial generation of ions, such as positively charged ions (H^+) and free electrons (e^-), which are the primary species produced during water radiolysis.

Due to the partial covalency of water's hydrogen bonding (see Appendix A), electrons are not held by individual molecules but are easily distributed amongst water clusters giving rise to coherent regions capable of interacting with ionizing radiation. The coherent state is a superposition where electron clouds oscillate between their individual ground configuration and an excited configuration where one electron per molecule is almost free, with binding energy of 0.4 eV [11].

Therefore, another important factor to consider when estimating the number of ions formed during the first stage of water radiolysis is the complex dielectric function of water, a function of the frequency of the applied electromagnetic field (ω). It can be expressed as:

$$\epsilon(\omega) = \epsilon_1(\omega) + i\epsilon_2(\omega), \quad (2.1)$$

where $\epsilon_1(\omega)$ and $\epsilon_2(\omega)$ are the real and imaginary parts of the dielectric function, respectively.

The real part of the complex dielectric function of water, which is dimensionless, is important in water radiolysis because it is directly related to the refractive index of water. The refractive index characterizes how light or electromagnetic radiation propagates through a medium, including water [12].

In the context of water radiolysis, the real part of the dielectric function influences the behavior of ionizing radiation as it interacts with water molecules. Specifically, it affects the absorption and transmission of radiation energy through the water medium.

The imaginary part is associated with the absorption and scattering of radiation within the water medium. It is expressed in m^{-1} and characterizes the energy dissipation and attenuation of radiation as it interacts with water molecules. It accounts for the absorption and scattering of radiation by water, which can result in the ionization of water molecules and the subsequent formation of reactive species [12].

At low frequencies and at room temperature, the real part of the dielectric function is relatively constant and has a value of approximately 78. At higher frequencies, $\epsilon_1(\omega)$ increases rapidly, reaching a maximum value of around 4000 at a frequency of about 22 THz. The imaginary part of the dielectric function is relatively small at low frequencies, but increases sharply at higher frequencies, indicating strong absorption and scattering of electromagnetic radiation by water molecules. The peak value of $\epsilon_2(\omega)$ occurs at around 20 THz, and is approximately 100 [13].

We will use the following example to estimate the number of ions formed in liquid water in this initial stage: an electron beam of area A impinges on the liquid water. Therefore, the number of ionizations will depend, as mentioned above, on the cross-section (σ) and the number of scattering centers (n) within a specific length Δx .

$$\Delta N_{ions} = \frac{n\sigma \Delta x A}{A} = n\sigma \Delta x \quad (2.2)$$

Based on the density of water, the Avogadro's number and the molar mass of water, the number of water molecules per cm^3 is computed. Numerical substitution was used to convert the cross section to Mb ($10^{-18} cm^2$) and the length to cm .

$$\Delta N_{ions} = \frac{6.02 \times 10^{-2}}{18} \sigma (Mb) \Delta x (cm) \approx \frac{1}{300} \sigma \Delta x \quad (2.3)$$

Therefore, converting Δx to nm , the number of ions per deposited energy is

$$\frac{\Delta N_{ions}}{\Delta x (nm)} = \frac{\sigma}{3} \quad (2.4)$$

Considering

$$\frac{\Delta N_{ions}}{\Delta x} = \frac{\Delta N_{ions}}{\Delta E} \frac{\Delta E}{\Delta x}, \quad (2.5)$$

where ΔE is the energy lost by the charged particle due to electronic collisions, we have:

$$\frac{\Delta N_{ions}}{\Delta E} = \frac{\frac{\Delta N_{ions}}{\Delta x}}{\frac{\Delta E}{\Delta x}}, \quad (2.6)$$

where $\frac{\Delta E}{\Delta x}$ represents the electron stopping power in water.

In other terms, we can express $\frac{\Delta N_{ions}}{\Delta E}$, also known as G-value, as

$$G(ions) = \frac{1}{3} \frac{\sigma (Mb)}{\frac{dE}{dx} (eV/nm)} \quad (2.7)$$

Figure 1, below, illustrates the stopping power of electrons in liquid water. After the Bragg peak, when the electron deposits most of its energy, the energy loss is roughly proportional to the inverse of the electron's energy. The energy of the electron when it first

enters the water is fixed, but as it loses energy over time, it deposits additional energy in succeeding stages. The electron stores almost all of its energy in a small area, known as the Bragg peak region, which is most vulnerable to radiation when the residual energy is around 100 eV [14].

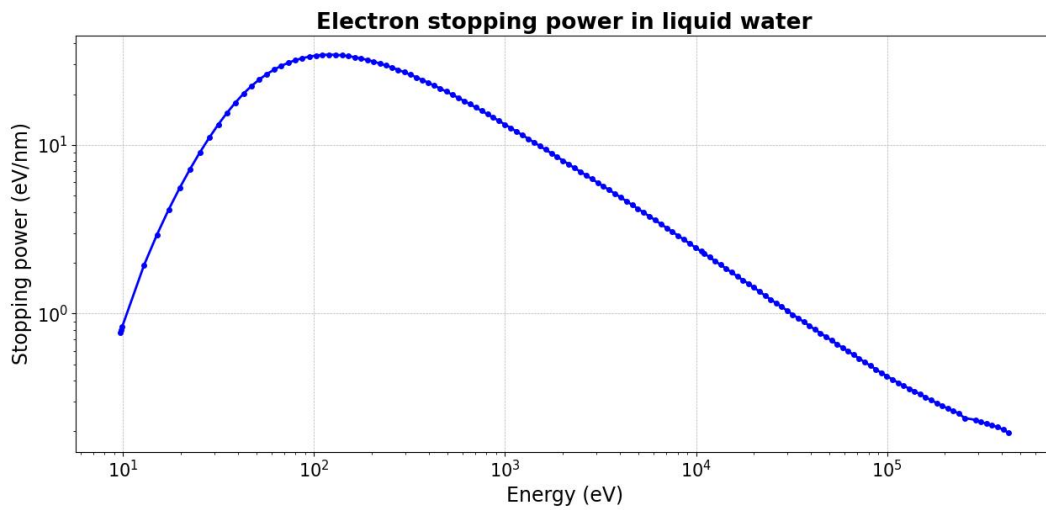


Figure 1 – Stopping power of electrons in liquid water. The Bragg peak is around 100 eV, which is the region where the most energy is deposited. Data taken from Castillo-Rico *et al.* [15].

Regarding electron cross-sections for water, we refer to the data obtained by Montenegro *et al.* [16]. The results were obtained by irradiating water vapor with an electron beam, and these results can be used in our example since this initial stage only concerns the interaction of radiation with water molecules and does not take into account the diffusion of products. The electronic energy levels of water are essentially the same in both the liquid and gaseous phases, and, therefore, the cross-sections are also the same.

The total of the cross-sections that create ions during the process yields the ionization cross-section. The number of expelled electrons, which become free in the medium and

go through a process of thermalization, serves as precursors for the creation of H_2 , and the quantity of created ions is proportional to the number of ejected electrons. These electron interactions with other radiolysis byproducts lead to the formation of H_2 .

Interactions with hydrated electrons, which are created from free electrons, lead to the formation of H_2 . The disparity between the quantity of ions and free electrons created during ionization is almost entirely due to the little amount of electrons that are captured by water molecules [17]. Therefore, the number of ions produced should be an upper limit for H_2 production. The quantity of H_2 generated at the end of the process is thus precisely proportional to the quantity of ions generated during the Physical stage.

Using the known parameters of stopping power and cross-section, we can estimate a G-value for the ions produced in this initial stage. We then compare the calculations with data obtained from Monte Carlo simulations [18, 19] and also experimental data [20] of H_2 produced at the end of the process, as shown in the Figure 2 below. From the plot, it is clear to see that the ions produced during Physical stage represent an upper limit to $G(H_2)$ yields at the end of Chemical stage.

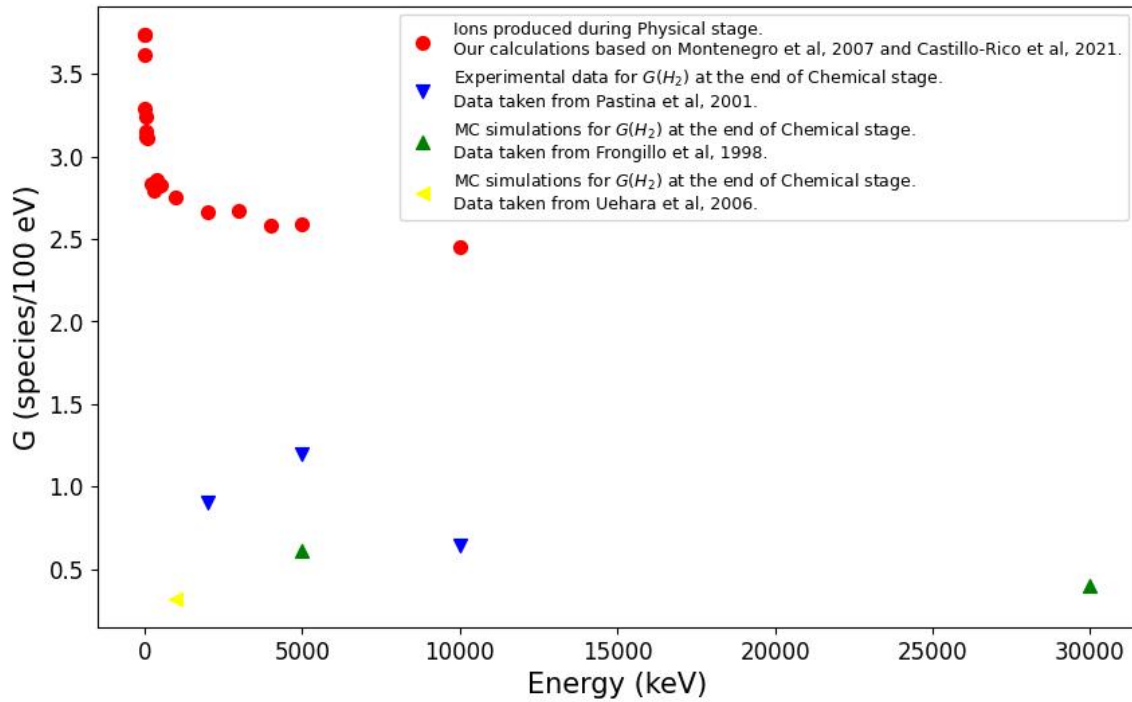
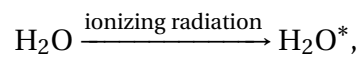
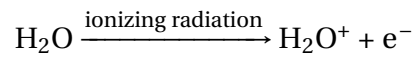


Figure 2 – Comparison between the estimated number of ions formed in the physical stage (red circles) with Monte Carlo simulations (up green and side yellow triangles) and experimental data (down blue triangles).

In summary, the interaction of ionizing radiation with water molecules describes this first step of water radiolysis, and the key products created are:



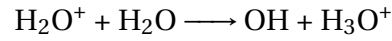
where H_2O^+ represents an ionized water molecule, H_2O^* represents an excited state water molecule, and e^- represents the electron ejected during ionization.

2.1.2 Physico-chemical stage ($10^{-15} - 10^{-12}$ s)

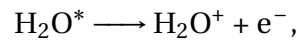
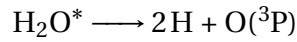
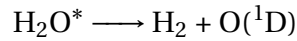
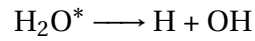
The species created during the Physical stage are highly unstable and can dissociate and diffuse. Among some of the events that occur in this second stage, it is worth noting the

transfer of protons to neighboring molecules, the dissociation of excited water molecules, and the thermalization of electrons.

The transfer of a proton to a neighboring water molecule results in:

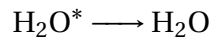


On the other hand, there are several channels for the dissociation of excited molecules:



where $O(^1D)$ and $O(^3P)$ are, respectively, the singlet and triplet states for the oxygen atom [21].

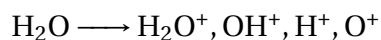
Additionally, it is possible for an excited molecule to return to its ground state through heat loss alone, without dissociating:



It is crucial to note that the dissociation of excited molecules' contribution to the synthesis of products at the conclusion of the Physical-Chemical stage is comparatively little because the number of excited molecules is significantly lower than the number of ionized molecules [17].

Ionized molecules

The molecules that are ionized during the Physical stage, as was already mentioned, also play a significant role in the Physical-Chemical stage. According to [22], the water molecule's potential fragmentation routes in the case of ionization include



The likelihood of removing electrons from the $1b_1$, $3a_1$, $1b_2$, and $2a_1$ orbitals of the water molecule affects the branching to fragmentation pattern of water. Vertical ionization energies for these orbitals are 12.61, 15.57, 19.83, and 36.88 eV, respectively. As electrons are removed from these levels, the emergence of the aforementioned channels [23], [24], and [25] becomes ever more favorable. A second electron may be ejected through the Auger effect when an electron is removed from the $2a_1$ orbital due to the large energy transfer involved. For more information, see Montenegro *et al.* [16].

The general fragmentation pattern for the water molecule's single and double ionization, as well as the corresponding probabilities, are shown in Figure 3.

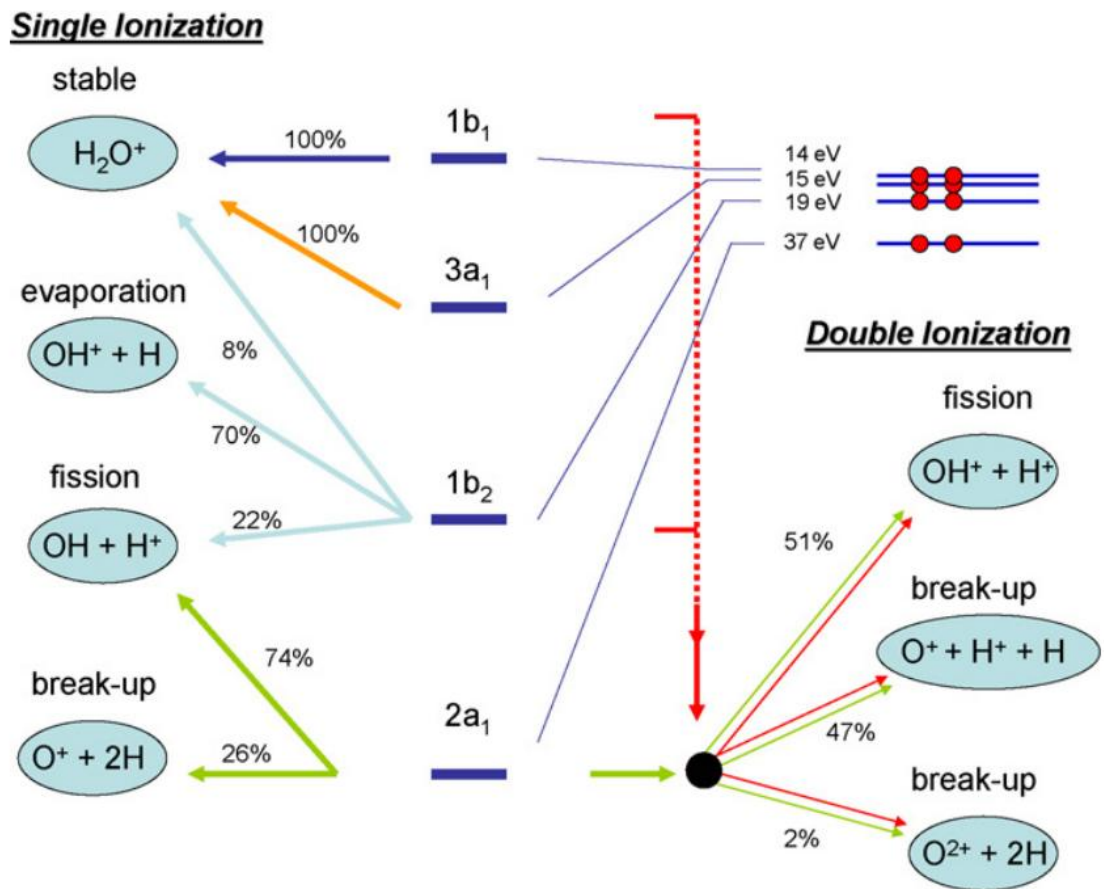
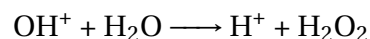
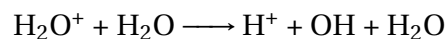


Figure 3 – Diagram representing the fragmentation pattern of water molecules under high-energy electron impact, resulting in single ionization and double ionization. Fig. taken from Montenegro *et al.* [16].

Upon formation, these ions interact with other species already present in the media to produce new products like:



Electrons

Electrons are ejected as a result of radiation ionizing water molecules. The thermalization process is subsequently applied to these expelled electrons. These electrons lose kinetic energy during this process, which continues until they attain thermal equilibrium

with the liquid water. After that, the water molecules, which are polar, meaning that they have a positive charge density surrounding the hydrogen atoms, interact with the electrons via electrostatic attraction, trapping them in a condition known as hydrated electron (e_{aq}^-). This condition exhibits the characteristics of a reactive chemical species and, as a result, lasts only for a brief time before it reacts with other species already present in the medium [26]. Despite its transient nature, the hydrated electron plays a significant role in water radiolysis, particularly in the creation of H_2 .

In what is known as the first hydration shell, each hydrated electron is typically surrounded by 6–7 water molecules; however, it is possible for it to be surrounded by as many as 23 water molecules in a second, shorter-lasting hydration shell. According to the Hartree-Fock and Kohn-Sham quantum models [27], Figure 4 depicts a similarity between the aqueous electron's molecular orbitals for each of these configurations. Although it lacks a spherical form and is exceedingly diffuse, the outermost occupied molecular orbital is frequently referred to as a *s*-type orbital. Similarly, the excitation process is seen as a $s \rightarrow p$ transition because the three lowest unoccupied orbitals have a roughly *p*-type symmetry. It is merely a rough approximation, though, and no true spherical symmetry is attained [28].

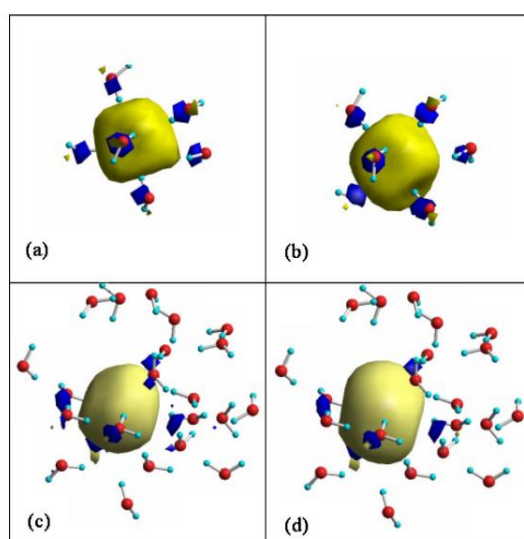


Figure 4 – Illustration of the molecular orbital of the hydrated electron. (a) and (b) represent, respectively, the Kohn-Sham and Hartree-Fock orbitals of the first hydration shell, while (c) and (d) represent the same orbitals for the second hydration shell. Figure retrieved from Ludwig, Coutinho and Canuto [28].

The yield (G-value) for each created species can be calculated at the conclusion of the Physico-Chemical stage, as shown in Table 1. It is crucial to stress that this ratio of species produced per 100 eV of deposited energy should be independent of the type and intensity of incident ionizing radiation because, following ion formation, subsequent reactions are solely dependent on the initial species and interactions in the aqueous medium rather than on radiation interaction [17].

G (molecules/100 eV)	OH	e_{aq}^-	H_3O^+	H	H_2	H_2O_2	OH^-	$O(^3P)$
Ionization	5,245	5,188	5,269			0,012		
Excitation	0,612	0,11	0,11	0,521	0,008	0,008		0,009
Recombination	0,109			0,204	0,041	0,041		0,048
Electron capture	0,081				0,081		0,081	
Total	6,047	5,298	5,379	0,725	0,13	0,061	0,081	0,057

Table 1 – Contributions from different mechanisms to the G-value for species present at time $t = 10^{-12}$ s for 150 keV electrons in liquid water. Data taken from Cobut *et al.* [17].

2.1.3 Chemical stage ($10^{-12} - 10^{-6}$ s)

There is a large range of potential reactions in the last step, known as the Chemical stage, which mostly depend on the number of species and their reaction rates. Some of these reactions are listed in Table 2, particularly those in which the creation of H_2 is directly or indirectly implicated.

Reaction	→	Product	Reaction rate constant k ($10^{10} dm^3/mol.s$)
(1) $OH + OH$	→	H_2O_2	0,6
(2) $OH + e_{aq}^-$	→	OH^-	2,5
(3) $OH + H$	→	H_2O	2,0
(4) $e_{aq}^- + e_{aq}^-$	→	$H_2 + 2OH^-$	0,55
(5) $e_{aq}^- + H$	→	$H_2 + OH^-$	2,5
(6) $e_{aq}^- + H_3O^+$	→	H	1,7
(7) $e_{aq}^- + H_2O$	→	$OH + OH^-$	1,3
(8) $H + H$	→	H_2	1,0
(9) $H + H_2O_2$	→	OH	0,01
(10) $H_3O^+ + OH^-$	→	H_2O	10

Table 2 – Reactions between the species present in the Chemical stage and their respective reaction rate constants k . Data taken from Uehara and Nikjoo [18].

Hence, it follows from Table 2 that H_2 is produced as a result of reactions (4), (5), and (8). The likelihood of reaction (8) occurring is the lowest of the group because it is more likely for a H atom to react with another species than with another H atom because the fraction of H in the aqueous medium is significantly lower than that of e_{aq}^- . Hence, it can be said that in the process of water radiolysis, the hydrated electron serves as the main precursor of H_2 [19].

As opposed to H_2 , however, the OH and H_2O_2 species interact with the e_{aq}^- to generate other species. As a result, these species are regarded as scavengers of the e_{aq}^- precursor because they reduce the quantity of H_2 generated by significantly lowering the e_{aq}^- concentration in the aqueous medium [10].

The concentration of H_2 generated by reactions (4), (5), and (8) is shown in Figure 5 as a function of time and varies according to the number of species and reaction rate:

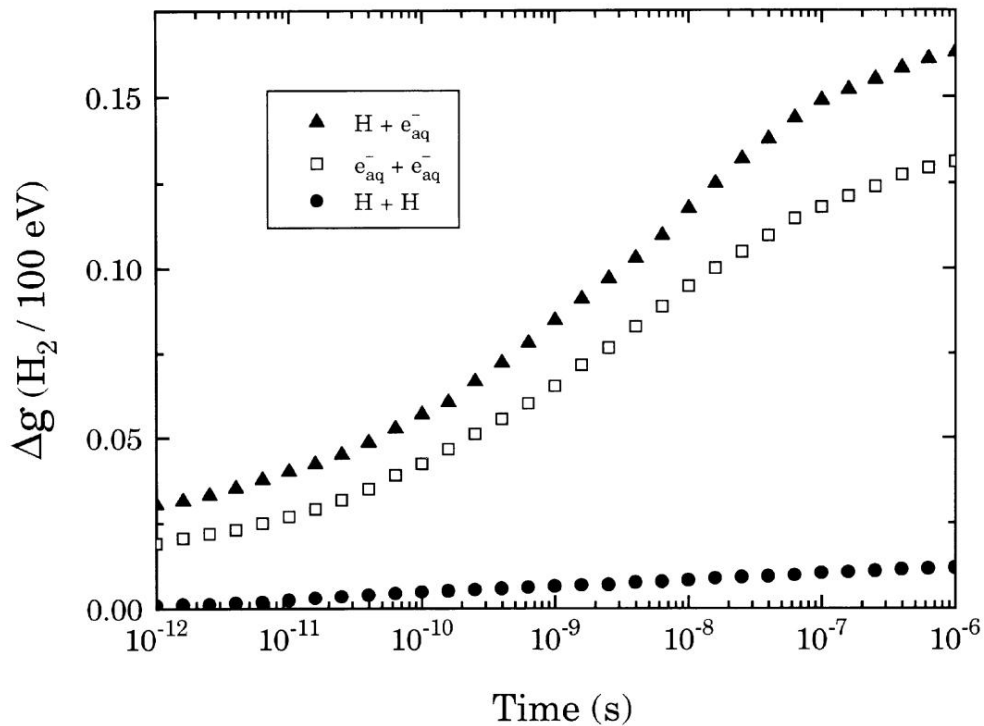
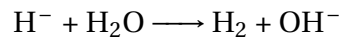
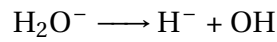


Figure 5 – Plot showing the temporal dependence of the reactions that lead to an increase in the production of H_2 . The significance of the reactions is quantified by the cumulative production variation (Δg) they cause. Figure extracted from Frongillo *et al.* [19].

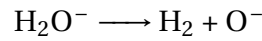
Additional research looks into the production of H_2 even in the absence of e_{aq}^- .

Although there is a significant drop, it is still conceivable to calculate a sufficiently high value of $G(H_2)$ to claim that all of the created H_2 is a result of reaction (8). According to Laverne and Pimblott [29], this generated H_2 should be the outcome of the interaction between other species and the free electron before it thermalizes. In this case, there would be electronic capture by a water molecule, forming a molecular anion.

From there, this anion could either directly disintegrate into molecular hydrogen or form a H anion, which would then produce molecular hydrogen through a quick reaction with a second water molecule.



or



As a result, at time $t = 10^{-6}$ s, at the conclusion of the Chemical stage, there would be a larger concentration of final products like H_2 and H_2O_2 and a lower concentration of transient species like e_{aq}^- and OH .

2.2 Photocatalytic water splitting

Water splitting on a semiconductor particle, such as titanium dioxide (TiO_2), involves the photoelectrochemical conversion of water into hydrogen and oxygen gases using light energy. The process is based on the principles of photocatalysis, which involves the acceleration of a chemical reaction by the absorption of light by a semiconductor material.

This phenomenon, also known as Honda-Fujishima effect, was first discovered in 1972 by Akira Fujishima and Kenichi Honda [30]. They observed that when titanium dioxide

was irradiated with ultraviolet light with an energy greater than its bandgap, electrons in the valence band absorb energy and get excited into the conduction band, leaving behind positively charged holes in the valence band. These electrons and holes can participate in various reactions. For example, in the presence of water, the holes can oxidize water to produce oxygen and protons, while the electrons can reduce the protons to produce hydrogen [30].

Fig. 6 shows a schematic diagram of water splitting into H_2 and O_2 over a heterogenous semiconductor photocatalyst. The three main processes in photocatalysis on semiconductor particles are as follows: (i) generation of electron-hole pairs in semiconductor particles as a result of photons absorbed at energies above the bandgap; (ii) charge separation followed by migration of these photogenerated carriers in semiconductor particles; (iii) surface chemical reactions between these carriers and various compounds (such as H_2O); electrons and holes may also recombine with each other without engaging in any chemical reactions [31].

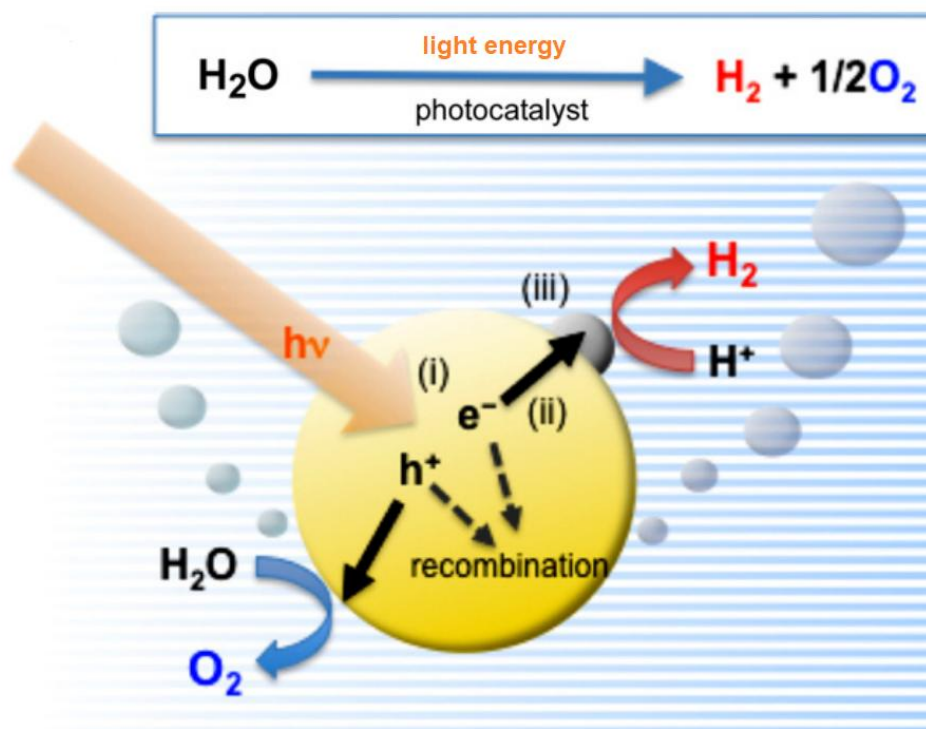


Figure 6 – Schematic illustration of water splitting over semiconductor photocatalyst. Figure taken from Abe [31] (see text for more information).

The mechanism behind the Honda-Fujishima effect can be summarized as follows:

1. Absorption of light: When a semiconductor particle is irradiated with light, the energy from the photons is absorbed by the electrons in the valence band of the semiconductor, causing them to jump to the conduction band and leaving behind holes in the valence band. Important points in the semiconductor photocatalyst materials are the width of the bandgap and levels of the conduction and valence bands. The bottom level of the conduction band has to be more negative than the redox potential of H^+ / H_2 (0 eV), while the top level of the valence band has to be more positive than the redox potential of O_2 / H_2O (1.23 eV), as Figure 7 shows.
2. Generation of electron-hole pairs: The absorbed energy generates electron-hole pairs in the semiconductor particle. The electrons are attracted to the particle surface, while the holes are attracted to the bulk of the particle. Crystal structure, crystallinity and particle size strongly affect this stage, as Figure 8 illustrates. The higher the crystalline quality, the smaller the amount of defects. The defects operate as trapping and recombination centers between photogenerated electrons and holes, resulting in a decrease in the photocatalytic activity. The probability of recombination decreases as particle size decreases because photogenerated electrons and holes have a shorter distance to travel to reaction sites on the surface.
3. Adsorption of water: Water molecules can adsorb onto the surface of the semiconductor particle, where they can react with the electron-hole pairs generated by the absorbed light.
4. Reduction and oxidation reactions: The electrons react with the adsorbed water molecules to produce hydrogen gas (H_2), while the holes react with other water molecules to produce oxygen gas (O_2).

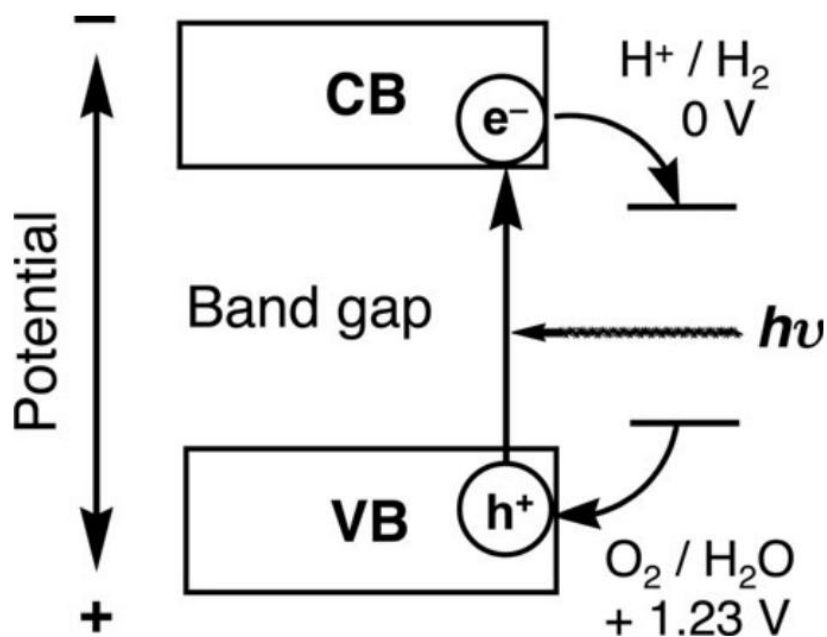


Figure 7 – Principle of water splitting using semiconductor photocatalysts. Figure taken from Kudo and Miseki [32].

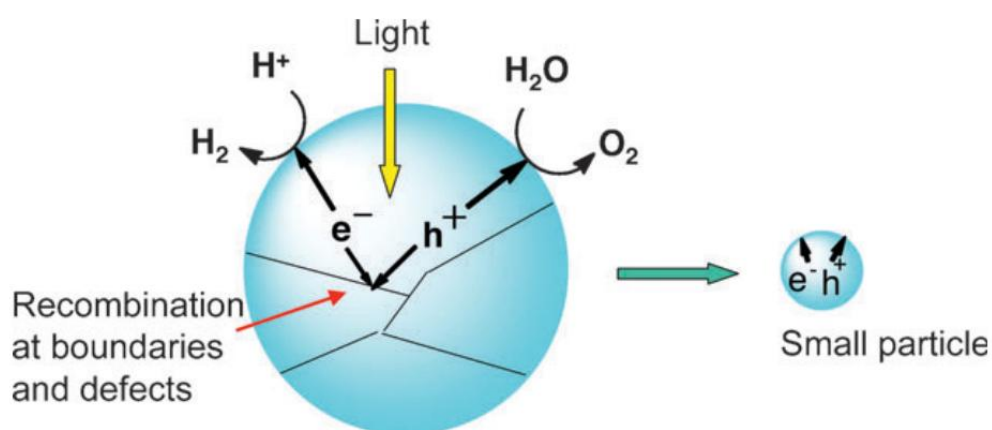


Figure 8 – Effects of particle size and boundary on photocatalytic activity. Figure taken from Kudo and Miseki [32].

The overall reaction can be represented by the following equation:



where $h\nu$ represents the energy of the absorbed light [31].

In addition to TiO_2 , other semiconductor materials, such as zirconium dioxide (ZrO_2) and silicon dioxide (SiO_2) can also be used for water splitting through photocatalysis [33].

Overall, water splitting on a semiconductor particle provides a promising method for producing hydrogen fuel from water using renewable energy sources, such as sunlight. It has the potential to become a key technology for achieving a sustainable and carbon-free energy future [5].

Chapter 3

Experimental Setup and Procedure

The construction of the experimental apparatus, the irradiation procedure, and the measurements will all be covered in this chapter. The experimental device was designed to function both as a container for liquid water and as a storage unit for the produced H_2 .

In this initial step, we will concentrate on characterizing the equipment and creating the best methodology for estimating the H_2 generated during the radiolysis of liquid water.

During the water irradiation, we have control over the amount of incident radiation, and it is possible to estimate the number of ions produced. After the approximately two-hour irradiation process, the amount of H_2 remaining in the container is determined using a mass spectrometry technique.

3.1 Irradiation chamber

The water to be irradiated in the liquid phase is placed in a container, known as the irradiation chamber, which is connected to a mechanical pump responsible for the removal of air. This chamber, shown in Figure 9, consists of a stainless steel cylinder with a diameter of 15.4 cm and a height of 21 cm. At the top, there is also a stainless steel ring that is pressed against the lid with the help of six screws to close the chamber, with an O-ring between them. The lid has an opening in the center, 6.5 cm in diameter, where a quartz cylinder is inserted to receive the radiation source, in this case a UV-C lamp. There is an air outlet connected to

the vacuum pump placed in the lid of the chamber, in order to more efficiently pump the leftover air out of the system. Therefore, this outlet connects the container not only to the vacuum pump, but also to a pressure gauge and another container, also made of stainless steel, responsible for storing the produced H_2 .



Figure 9 – Sealed irradiation chamber coupled to a vacuum pump, with a UV-C lamp irradiating a water sample.

Portable chamber

During the execution of the experiments, we encountered some difficulties, particularly due to the COVID-19 pandemic, which delayed the completion of the assembly of the LMS (Laboratório Mansukh Shah) laboratory at Universidade Federal Fluminense (UFF). Under these circumstances, we had the idea to connect the irradiation chamber to another chamber, which is quite small and therefore portable, solely for storing the H_2 produced in water radiolysis. After the air is pumped out and irradiation begins, a valve connected to the air outlet linked to the vacuum pump is closed, sealing the system so that there is a

connection only between the two containers. This new container, shown in Figure 10, has an outlet linked to the whole system, connected to a valve that is closed at the end of the irradiation to store and transport the H_2 to LaCAM, located at Universidade Federal do Rio de Janeiro (UFRJ), where the mass spectrometer, to be described later as the measurement system, is located.



Figure 10 – Portable chamber responsible for the storage and transport of H_2 produced in water radiolysis.

3.2 Vacuum system

Mechanical vacuum pump: The mechanical vacuum pump to be used is an *Edwards* belt-driven vacuum pump; it has the capacity to maintain a chamber with the above-described volume at a pressure of 10^{-2} mbar. The pump is connected to the apparatus before irradiation, as the removal of air from the container is vital for obtaining good measurements, once that the amount of H_2 produced during radiolysis is much less than the number of air molecules under atmospheric pressure.

Pressure gauge: The pressure gauge used to monitor the pressure inside the chamber was a *Pfeiffer Vacuum TPR 280 Series Pirani Gauge*, capable of measuring pressures between 100 to 10^{-3} hPa.

With the pressure gauge connected to the system, we repeatedly performed vacuum tests over several days. First, the chamber was emptied and cleaned so that there were no residues, as shown in Figure 11, and pumped for five minutes to remove air. Under these circumstances, the measured pressure reached the order of 10^{-1} Torr, indicating that there were no sizeable leaks.



Figure 11 – Empty and clean chamber before irradiation.

Afterwards, we conducted vacuum tests with the introduction of a new variable to the system, liquid water at room temperature. Since the radiation source used was a UV-C light lamp, whose penetration range in liquid water is usually less than a millimeter, a small amount of water would be sufficient to observe the phenomenon. However, the need to create a low-pressure environment in the container determines the amount of water involved. If the water level is too low, the water could be completely evaporated due to low pressure or sucked up by the vacuum pump. Under this condition, the identified pressure was around 5 Torr, which indicates an appropriate low-pressure scenario for water radiolysis. Pumping for longer

to reach even lower pressures would not bring advantages to the experiment, since much of the air has already been removed and the pressure variation becomes small, indicating that the system has reached a certain equilibrium.

3.3 Radiation source

After the air is removed, the liquid water reaches thermal equilibrium with the environment, and the irradiations begin. The equipment used as a radiation source is a commercial UV-C lamp, used as a source of ultraviolet light (*OSRAM PURITEC HNS 9W G23* low-pressure model). The lamp is 14.2 cm long and 2.8 cm in diameter. It is a mercury lamp that provides light with a wavelength of 253.71 nm. As mentioned earlier, ultraviolet light in this wavelength range between 100-280 nm has a short penetration depth in liquid water, less than a millimeter, and is almost immediately absorbed when incident on an aqueous medium.

This low-pressure mercury-vapor lamp operates by creating an electric discharge in a low-pressure environment filled with mercury vapor. Here is more detailed description of the process:

1. Electric discharge: When the lamp is turned on, an electric current is applied to the mercury vapor within the lamp. This electric current is typically initiated via electrodes at the ends of the lamp.
2. Excitation of mercury atoms: The electric current excites the mercury atoms, causing the electrons in the mercury atoms to jump to higher energy levels (or excited states). This is a short-lived state, and the electrons quickly return to their original energy levels.
3. Emission of UV light: When the electrons drop back to their original energy levels, the energy difference is released in the form of ultraviolet light, specifically in the UV-C range (100-280 nm). In the case of mercury-vapor lamps, the most intense line occurs at a wavelength of 253.71 nm.

4. Production of visible light: Some visible light is also produced in this process, but low-pressure mercury-vapor lamps are designed to minimize this since the primary aim is to produce UV-C light.

Therefore, this wavelength provides a maximum energy of:

$$E = \frac{hc}{\lambda} = \frac{6.626 \times 10^{-34} \text{ Js} * 3 \times 10^8 \text{ m/s}}{253.71 \times 10^{-9} \text{ m}} = 7.83 \times 10^{-19} \text{ J} = 4.89 \text{ eV}, \quad (3.1)$$

which is greater than the thermodynamic potential difference necessary for liquid water splitting to occur under standard conditions, which corresponds to an energy of 1.23 eV. This is essentially the energy required to overcome the chemical bonds in water, separating it into hydrogen and oxygen.

Quartz cylinder

In the context of UV-C lamps systems, a quartz cylinder is often chosen to encase the lamp for several reasons:

1. Transparency to UV-C light: Quartz is highly transparent to UV-C radiation, allowing virtually all the UV-C light emitted by the lamp to pass through it and interact with the surrounding environment. This is not the case with most types of glass, which absorb UV-C light and would therefore block the lamp's radiation.
2. Thermal Stability: Quartz has excellent thermal stability, allowing it to withstand the heat generated by the lamp without cracking or deforming.
3. Chemical Inertness: Quartz is chemically inert, meaning it won't react with the lamp or the environment, which is particularly important if the lamp system is being used in a sensitive context such as water radiolysis.
4. Mechanical Strength: Quartz is a hard and durable material that provides a strong, protective casing for the lamp.

Therefore, when using a UV-C lamp where the radiation needs to interact directly with the environment, encasing the lamp in a quartz cylinder is an excellent choice to maximize the effectiveness of the lamp and protect it from the water environment at the same time [32].

3.4 Semiconductor materials

As mentioned before in Section 2.2, semiconductor materials play a crucial role in enhancing H_2 yields through water radiolysis. In particular, they can effectively absorb UV-C photons and generate electron-hole pairs, initiating the water radiolysis process. UV-C radiation carries higher energy photons compared to visible or longer wavelength ultraviolet light. This higher energy can result in more energetic electron-hole pairs being generated in the semiconductor material.

For these first experiments, two types of semiconductor materials in nanoscale particles, titanium dioxide and silicon dioxide, were used in order to compare their efficiency as photocatalysts for H_2 production. These two materials are economically viable for acquisition, and their properties are described below.

Titanium dioxide

Titanium dioxide is composed of titanium (Ti) and oxygen (O) atoms, with a chemical formula of TiO_2 . It can exist in different crystalline structures, including rutile, anatase, and brookite, as Figure 12 illustrates. The specific crystal structure affects its physical and chemical properties. Anatase and rutile are the most commonly encountered crystal structures for TiO_2 nanoparticles. Anatase nanoparticles tend to be more reactive and exhibit higher photocatalytic activity compared to rutile nanoparticles. Rutile nanoparticles, on the other hand, generally have better thermal stability and lower photocatalytic activity but can still exhibit some photocatalytic properties [34].

Brookite is less commonly found in TiO_2 nanoparticles compared to rutile and anatase. It is the least stable among the three crystalline forms and is typically transformed into

rutile or anatase during the synthesis or annealing processes. In our experiments, anatase TiO_2 was used and it appears as a white powder with a tetragonal crystal structure. It has a wide bandgap energy of 3.2 eV, which allows it to absorb UV-C radiation effectively [34].

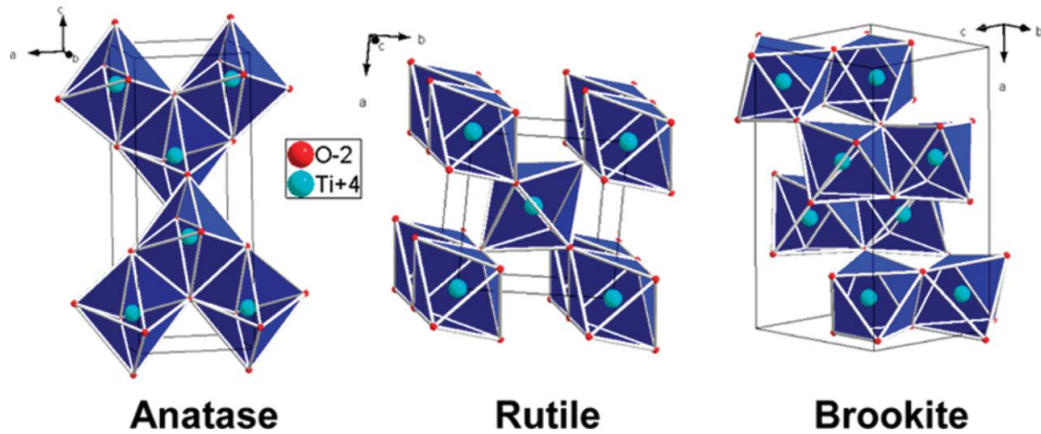


Figure 12 – Representations of the TiO_2 anatase, rutile, and brookite forms. Figure taken from Dambournet *et al.* [34].

Upon UV-C light absorption, TiO_2 generates electron-hole pairs. Efficient charge separation and transfer are crucial for successful photocatalysis. Titanium dioxide's particular electronic structure allows for efficient separation and migration of electrons and holes, preventing their recombination. This enhances the overall efficiency of the photocatalytic process. Besides, titanium dioxide is known for its stability and durability, which are essential for long-term photocatalytic applications. It can withstand harsh reaction conditions, including ionizing radiation, high temperatures, and chemical environments. This stability ensures prolonged and efficient H_2 production through water radiolysis using UV-C light [34].

Silicon dioxide

Silicon dioxide is composed of silicon (Si) and oxygen (O) atoms, with a chemical

formula of SiO_2 . It exists in several crystalline forms, including quartz, cristobalite, tridymite, and amorphous (non-crystalline), as shown in Figure 13. Amorphous silicon dioxide lacks long-range atomic ordering and has a disordered structure. It is commonly encountered in the form of a transparent glassy material or a white powder, and the last form is the one we used in our experiments. In this specific form, SiO_2 can absorb ultraviolet light and therefore increase photocatalytic activity [35].

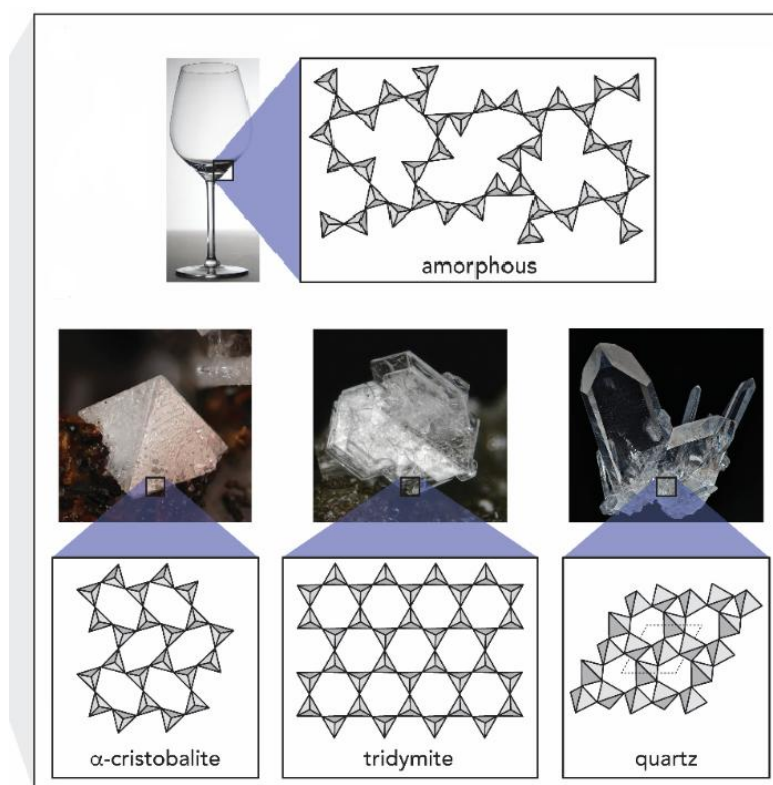


Figure 13 – Different arrangements of silicon dioxide, including amorphous SiO_2 and other examples of different polymorphs of crystalline SiO_2 : cristobalite, tridymite and quartz. Figure adapted from Moura and Unterlass [35].

Even though modifications can enhance its photocatalytic activity to some extent, SiO_2 is generally considered less efficient than other materials like TiO_2 for water splitting reactions, since silicon dioxide does not possess the necessary band structure or energy levels to efficiently absorb UV-C light for initiating water radiolysis.

3.5 Mass spectrometer (TOFMS)

After irradiating the water and storing the resulting H_2 , the portable chamber is taken for measurement using a Time-Of-Flight (TOF) mass spectrometer. The mass spectrometer is located in the electron collisions laboratory at UFRJ.

Figure 14 shows a schematic of the experimental setup, including a collision region (interaction region), along with a pulsed electron gun connected to a gas cell and a time-of-flight (TOF) drift tube, as well as an Einzel-like lens assembly. When an electrostatic extraction field is used to direct the ions towards the TOF drift tube in electron-gas collision studies, pulsed electron beams are frequently used in order to prevent beam deflection. After the TOF, a Micro-Channel Plate (MCP) detector is used to collect the positively charged ions and ionic fragments generated in the collisions between the electron target gas and electrons. To guarantee a single-collision regime for gas samples, the gas cell is maintained at a maximum working pressure of 3.0×10^{-4} Torr, where the projectiles impact with the target gas. The number of scattering centers in the interaction zone can be determined by measuring the gas cell pressure using an absolute capacitive manometer (a *MKS Baratron*), and the electrons in the electron beam are collected by a Faraday cup that is placed after the gas cell. In order to prevent stray magnetic fields from deflecting the electron beam as it passes through the gas cell, Mu-metal cylinders are employed.

A home-made electron gun that operates in the 20–1000 eV energy range and has an average energy resolution of 0.5 eV generates the electron beam. A tungsten filament, a set of aligning deflection plates in front of a 0.5 mm collimator, five cylindrical focusing accelerating electrodes, and a second set of steering deflection plates at its end for fine-tuning the beam's direction are all components of the device. The beam then passes through a 0.8 mm collimator at the gas cell's entrance. In order to deflect the beam within the gun and let it pass through the collimator only when the pulse is off, both sets of aligning deflection plates placed before the gun's collimator are given a 5 V potential in order to pulse the beam [36].

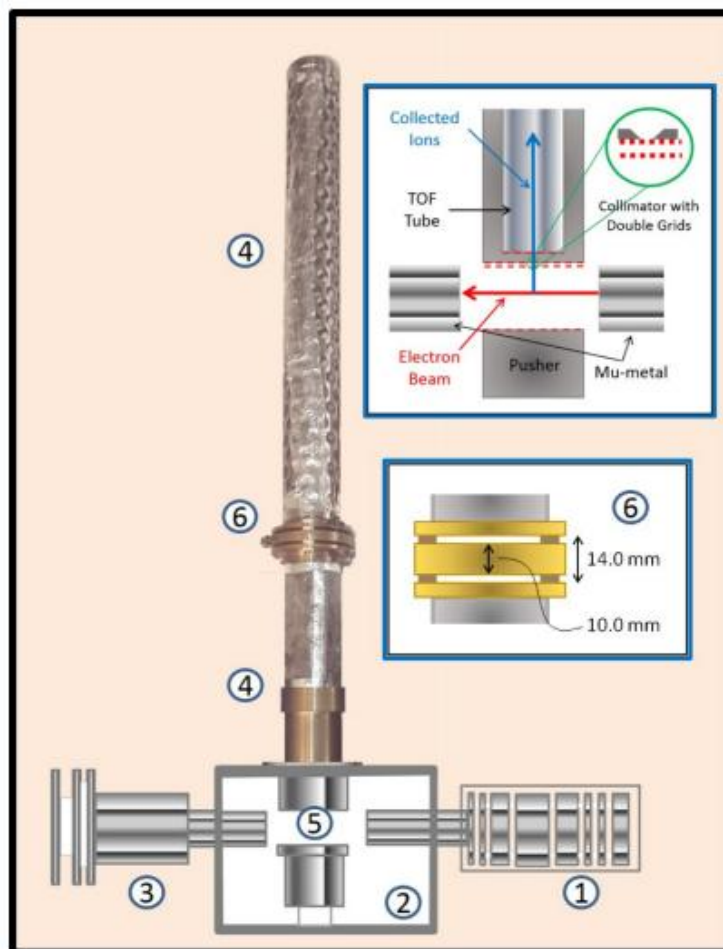


Figure 14 – Illustration of the experimental configuration, showing the electron gun (1), the gas cell (2), the Faraday cup (3), and a picture of the TOF drift tube (4). The Mu-metal cylinders, the grids (shown by red traced lines), and a zoom of the conical collimator to the TOF drift tube are all seen in the inset above's detailed schematics of the interaction zone (5). The horizontal red arrow denotes the electron beam, and the vertical blue arrow denotes the recoiling ions. The spacing between the Einzel-like lens's components, which are segregated by ceramics, is depicted in the inset schematic of the lens (6) below (also represented). Figure taken from Sigaud *et al.* (2016) [36].

The typical setup for the tests that are being presented uses electron beam pulses that are 50 ns long and 20 kHz in frequency. After the electrons have passed, a pulsed extraction electrostatic potential of 300 V with a rising time of 100 ns is applied to the pusher electrode in order to direct the positively-charged ions and molecules produced inside the TOF drift tube at a distance of about 6.0 mm from the collimator towards the MCP. This produces

a field of about 21 V/mm across the interaction region. A stop signal is given by the MCP once a charged fragment arrives, resulting in a mass-to-charge ratio discriminated spectrum. The extraction field pulse is produced in synchronism with the electron beam pulse with an adjustable delay time between them. It provides the start signal to the acquisition electronics while it is being fed to the pusher's 300 V power source [36].

The gas cell has a volume large enough to guarantee exuberant laminar flow of the gas through the cell apertures and pressure stability. Its dimensions are 64.2 mm x 55.0 mm x 110.0 mm. To achieve the greatest level of control over the gas flow into the target cell, the gas intake line is managed by a double set of needle valves. As a result, the number of scattering centers can be precisely regulated and calculated. In order to achieve a number density of $n_c \approx 10^{13}$ scattering centers per cm^3 inside the gas cell, effusive flow from the target cell through the beam entrance and the target product extraction apertures results in a differential pressure ratio of 1/100 between it and the main chamber.

The extractor assembly consists of a grounded copper plate above the interaction region and a cylindrical metal grid with a 60° conical aperture that is 6.0 mm in diameter facing the TOF drift tube. The purpose of this conical aperture was to eliminate any potential lines that might have formed between the grounded upper extraction plate and the start of the TOF drift tube grid, which were separated by 4.6 mm. The ions or charged molecule fragments inside the TOF drift tube can be focused with the aid of this so-called electrical lens. The extractor and TOF drift tube voltage differential determines the focus position. In order to further focus the ions and ionic molecular fragments and reduce losses inside the long drift tube, an Einzel-like lens is installed at one third of the TOF tube length. The TOF drift tube was found to work best at -2000 V and the Einzel lens at 1000 V for focusing the extracted ions. Before the conical aperture, there is a double set of gratings whose purpose is to stop stray electric fields from the TOF tube from interfering with the collision and extraction procedures.

The detection efficiency of the target fragment ions by the MCP detector depends heavily on how energetically they strike the detector's front surface. Changing the voltage

applied to the detector's front surface changes the energy of the impacting ions. When this voltage was changed from -2900 V to -3100 V, no appreciable change in the recorded single to double ionization cross-section ratios was seen. The consistency of the single to double ionization cross-section ratios suggests that singly ionized products are also detected with constant efficiency since doubly ionized products acquire twice as much energy as singly ionized products and hence have a significantly better detection efficiency [37].

The 476 mm long TOF tube, which has meshes on both ends with a 30 mm diameter, is traversed by the ions. Figure 14 further shows that the TOF tube is completely perforated with holes to ensure that its inside is equally pumped as the tube's entrance is one of the cell's only gas exits and is covered in a mesh to prevent electrical field leakage. The detector, a 40 mm diameter Quantar resistive anode position-sensitive MCP detector, is kept at a -3300 V potential at a 20.0 mm distance from the end of the TOF tube. The end of the TOF tube is 3.0 mm distant from a grounded grid (at a 17.0 mm distance from the MCP). This grid's inclusion aids in maintaining an even electrical field between the TOF drift tube and the MCP surface, minimizing any potential undesirable lens effects close to the detector [36].

The signal from the MCP detector is fed into a standard data acquisition electronics (see Figure 15), consisting of an amplifier and a constant fraction discriminator (CFD). The detector pulses are used as stop pulses to a time-to digital converter (TDC) analyser, and pulses derived from the extraction pulser are used as start pulses. A second gate and delay between the extraction pulse and the TDC is needed in order to avoid the noise generated by the extractor pulser. This choice is crucial to synchronize the pulses with the ion pusher, allowing the fragments to be separated based on their respective mass-to-charge ratios. The ion pusher's pulse serves as the start signal for the data acquisition electronics, and each pulse counted upon an ion's arrival at the detector corresponds to a stop signal for the same electronics. As a result, we can precisely separate the different ionic fragments based on their mass-to-charge ratio and the time it takes for each fragment to reach the detector [37].

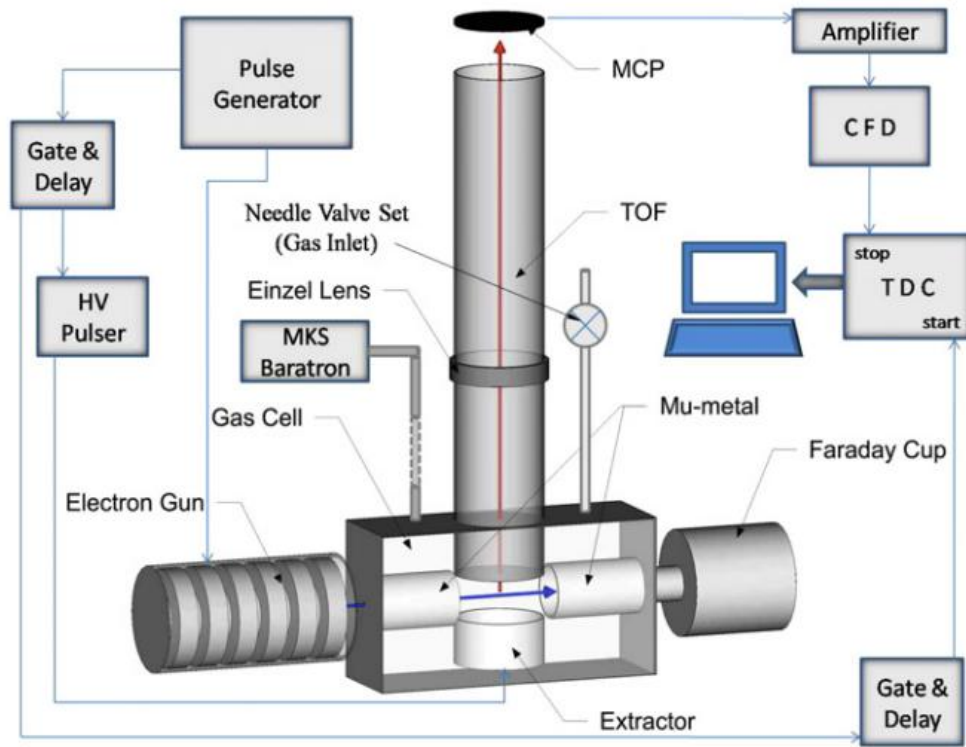


Figure 15 – Experimental setup, showing the electron gun, the gas cell, the Faraday cup, the MCP detector, the TOF drift tube, the gas inlet system and the data acquisition electronics. Figure taken from Sigaud *et al.* (2010) [37].

This apparatus and methodology enable, therefore, the investigation of the mechanism of H_2 formation in water radiolysis, by knowing the number of incident electrons n_e , the number of scattering centers of the gas target n_c , the dimensions of the interaction region d , and the absolute detection efficiency ϵ , absolute ionization and fragmentation cross sections (σ) for each process can be obtained

$$\sigma = \frac{N}{n_e n_c \epsilon d}, \quad (3.2)$$

where N is the number of recorded events in the TOF spectrum for each particular collision process [36].

Chapter 4

Results discussion and implications

This chapter evaluates the experimental setup and methodology used to explore H_2 production in water radiolysis, as well as the outcomes of the measurements.

The experimental measurements are analyzed quantitatively, drawing inspiration from data and procedures found in the literature.

It was necessary to measure the residual gas in the non-irradiated container, or the experiment's background measurement, in order to use the water molecule as a point of comparison. The ratio between the present species and the water molecule forms the fundamental structure of our data.

4.1 Background measurement

In all scenarios, we used 1.5 L of water inside the irradiation chamber. Initially, the container with this amount of non-irradiated water in thermal equilibrium with the environment was analyzed on the mass spectrometer after the same measurement time as the irradiations, which is 600s. This prior measurement aims to identify the molecules present in the container before irradiation and quantify the water molecule for post-irradiation normalization.

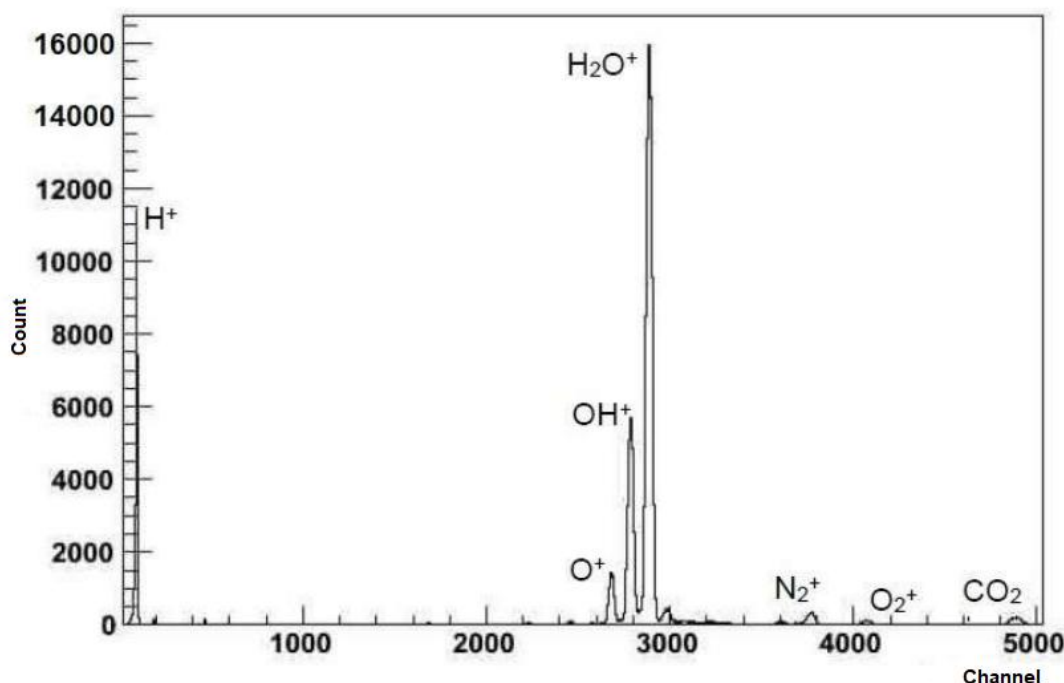


Figure 16 – Background spectrum of the experiment, container with non-irradiated water (measurement time 600s).

In the spectrum shown in Figure 16, the predominant presence of the water molecule is clearly noticeable. However, we should investigate the presence of secondary molecules, which originate from the ionization of the H_2O molecule followed by its dissociation. Depending on the molecular orbital from which this electron was ejected, the water molecule may dissociate when it interacts with the electron beam from the electron gun in the mass spectrometer and produce other ions that will be measured (see Appendix A).

The electrons from the ionizer beam have an energy of 100 eV, and the cross sections[†] for the production of each ion show us that the predominantly produced fragments are: H_2O^+ , OH^+ , O^+ , and H^+ [16].

The presence of other molecules such as O_2 , N_2 and CO_2 may originate from a residual amount of air remaining in the container. However, the first two species do not influence the measurement of H_2 . On the other hand, the presence of CO_2 can potentially influence

[†]Estimated non-systematic uncertainties are 2% for H_2O^+ , 3% for H^+ , 5% for OH^+ and 7% for O^+ [16].

H_2 measurements, therefore the amount of carbon dioxide will also be normalized by the amount of water. CO_2 , present in air, when present in the system, can interact with species produced by water radiolysis and alter the dynamics of the resulting chemical reactions.

The area under the peaks for each species in Figure 16 is calculated and normalized by the area under the H_2O peak, as was mentioned above, in order to analyze the data.

Each individual ion's area is proportional to the cross section of the ion generation during the bombardment of the water molecule with 100 eV electrons from the TOFMS electron gun. Then, we can compare the outcomes of our experiments with data from Montenegro *et al.* [16], as shown in Table 3.

Ratios	H_2^+ / H_2O^+	H^+ / H_2O^+	O^+ / H_2O^+	OH^+ / H_2O^+
Ratios between cross sections at 100 eV [16].	0.0015	0.253	0.049	0.303
Ratios between measurements in TOFMS with non-irradiated water.	0.0013	0.719	0.062	0.375

Table 3 – Comparison of the ratios between the cross sections from reference [16] and the ratios between the measurements of the background spectrum.

Our measurements of the H_2^+ , OH^+ and O^+ ions agree with the ratios between the cross sections, showing that the dissociation of the water molecule is the direct cause of these fragments.

The only discrepancy lies in the comparison of data for the H^+ ratio, but this difference can be explained by various factors such as the detection efficiency of the spectrometers. Due to their exceptionally light mass, H^+ generates weaker signals in many detectors, making its detection more difficult, especially at low concentrations.

4.2 Theoretical predictions of measured molecules

The number of molecules leaving the container and entering the TOFMS gas cell is analyzed considering water as an infinite medium, while the produced H_2 is finitely limited. During the measurement period, the water is in the liquid phase in a low-pressure environ-

ment and some of its molecules transition from the liquid to the gaseous phase. Therefore, The system can be thought of as an environment with varying concentrations of H_2 and H_2O .

The collision rate per unit of time per unit of area, a , and the effective area of the needle valve, S , which serves as the entrance to the TOFMS gas cell, are directly proportional to the number of H_2 molecules leaving the chamber per unit of time. Therefore,

$$\frac{dN_{H_2}}{dt} = -aS \quad (4.1)$$

The collision rate per unit of time per unit of area is

$$a = n\sqrt{\frac{k_B T}{2\pi m}}, \quad (4.2)$$

where n is the number of molecules of that species per unit volume, k_B is the Boltzmann constant, T is the temperature of the system, and m is the mass of the species.

Then,

$$\frac{dN_{H_2}}{dt} = -\frac{N_{H_2}}{V}\sqrt{\frac{k_B T}{2\pi m_{H_2}}}S = -\frac{N_{H_2}}{\tau}, \quad (4.3)$$

where τ is a constant that can be defined as:

$$\tau = \frac{V}{S\sqrt{\frac{k_B T}{2\pi m_{H_2}}}} \quad (4.4)$$

Integrating equation (4.3), we obtain the dependence on the number of H_2 molecules that remain in the target over time,

$$N_{H_2}(t) = N_0 e^{-\frac{t}{\tau}}, \quad (4.5)$$

where N_0 is the total number of H_2 produced in the chamber.

The electron beam from the electron gun will, however, only interact with a very small portion of the H_2 molecules that exit the chamber, pass through the needle valve, and enter the TOFMS gas cell. According to the cross section (σ_{H_2}) for the production of H_2^+ by 100 eV electrons impinging on H_2 , only a small amount (γ) of these molecules will be ionized. As a result, the rate of ionized H_2 molecules per unit of time is:

$$\frac{dN_{H_2^+}}{dt} = \gamma a S \sigma_{H_2} = \gamma \frac{N_{H_2}}{V} \sqrt{\frac{k_B T}{2\pi m_{H_2}}} S \sigma_{H_2} \quad (4.6)$$

In other words,

$$\frac{dN_{H_2^+}}{dt} = \frac{N_0 e^{-\frac{t}{\tau}}}{\tau} \gamma \sigma_{H_2} \quad (4.7)$$

By integrating equation (4.7), we obtain the number of H_2 molecules measured in the spectrometer at a given time t

$$N_{H_2^+} = N_0 \gamma \sigma_{H_2} \left[1 - e^{-\frac{t}{\tau}} \right] \quad (4.8)$$

Assuming that water is an infinite medium, we can say that the amount of water in the chamber can compensate for the removal of water molecules by the needle valve, maintaining partial pressure without significantly changing volume. As a result, we can say that the number of H_2O molecules leaving the target per unit of time is independent of time. This amount is determined by multiplying the area of the needle valve, S , by the collision rate per unit of time per unit of area, A .

Thus, N_{H_2O} depends only on the partial pressure (p_{H_2O}), the volume of the container (V), and the temperature of the system (T). By the ideal gas equation, we have that $N = \frac{p}{k_B T}$. Therefore,

$$N_{H_2O} = \frac{p_{H_2O}}{k_B T} \sqrt{\frac{k_B T}{2\pi m_{H_2O}}} S \quad (4.9)$$

And the ratio of ionized H_2O molecules per unit of time is

$$\frac{dN_{H_2O^+}}{dt} = \frac{p_{H_2O}}{k_B T} \sqrt{\frac{k_B T}{2\pi m_{H_2O}}} S \gamma \sigma_{H_2O} \quad (4.10)$$

By integrating equation (4.10), we obtain the number of H_2O molecules at a given time t ,

$$N_{H_2O^+} = \frac{p_{H_2O}}{k_B T} \sqrt{\frac{k_B T}{2\pi m_{H_2O}}} \gamma \sigma_{H_2O} t \quad (4.11)$$

We calculate the ratio between the number of H_2 molecules and the number of water molecules that the TOFMS will measure using equations (4.8) and (4.11):

$$\frac{N_{H_2^+}(t)}{N_{H_2O^+}(t)} = \frac{N_0 \gamma \sigma_{H_2} \left[1 - e^{-\frac{t}{\tau}} \right]}{\frac{p_{H_2O}}{k_B T} \sqrt{\frac{k_B T}{2\pi m_{H_2O}}} S \gamma \sigma_{H_2O} t} \quad (4.12)$$

In other words,

$$\frac{N_{H_2^+}(t)}{N_{H_2O^+}(t)} = \frac{N_0 k_B T}{p_{H_2O} V} \left(\frac{\sigma_{H_2}}{\sigma_{H_2O}} \right) \left(\sqrt{\frac{m_{H_2O}}{m_{H_2}}} \right) \frac{\left[1 - e^{-\frac{t}{\tau}} \right]}{(t/\tau)} \quad (4.13)$$

It is clear from equation (4.13), however, that the decay of the ratio of H_2^+ to H_2O^+ ions is caused by the time constant τ . The magnitude of the time it takes for the H_2 molecules to exit the chamber and enter the TOFMS gas cell will be determined by this parameter.

As a result, N_0 , or the total number of H_2 molecules in the chamber, is the only free parameter. Monte Carlo simulations can be used to estimate this number, which is related to $G(H_2)$ (see Chapter 2). To demonstrate the decay of H_2 production over time, we conducted 5

measurements during 500 seconds using the TOF mass spectrometer during 2 hours and 4 hours of irradiation on pure liquid water, as shown in Fig. 17.

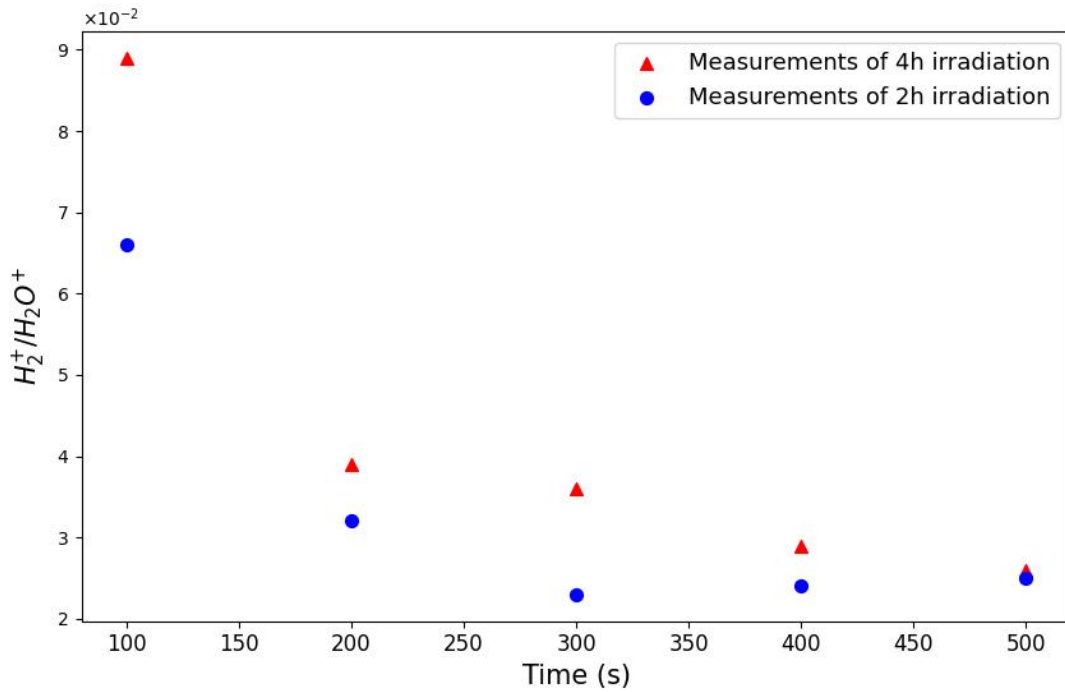


Figure 17 – Plots depicting the amount of H_2 as a function of time, normalized by the quantity of H_2O in the system.

4.3 Post-irradiation experimental results

In this work, irradiations were performed for 2 hours each for different scenarios: pure water, water with SiO_2 , and water with TiO_2 . Inspired by McGrady *et al.* [38], we carried out measurements for different proportions between the liquid water and the semiconductor materials used as photocatalysts. In each instance, we maintained the volume of water at 1.5 L, while manipulating the volume of the photocatalyst used. Specifically, we conducted trials with photocatalyst volumes of 15 mL, 30 mL, and 45 mL respectively. This strategy allowed us to study the impact of the photocatalyst's volume on the overall experiment and provided us with diverse data for comparative analysis. It took the TOFMS 600 seconds to complete its measurements of the gas samples and the ratios between H_2^+ and H_2O^+ were plotted, as shown in Figure 18.

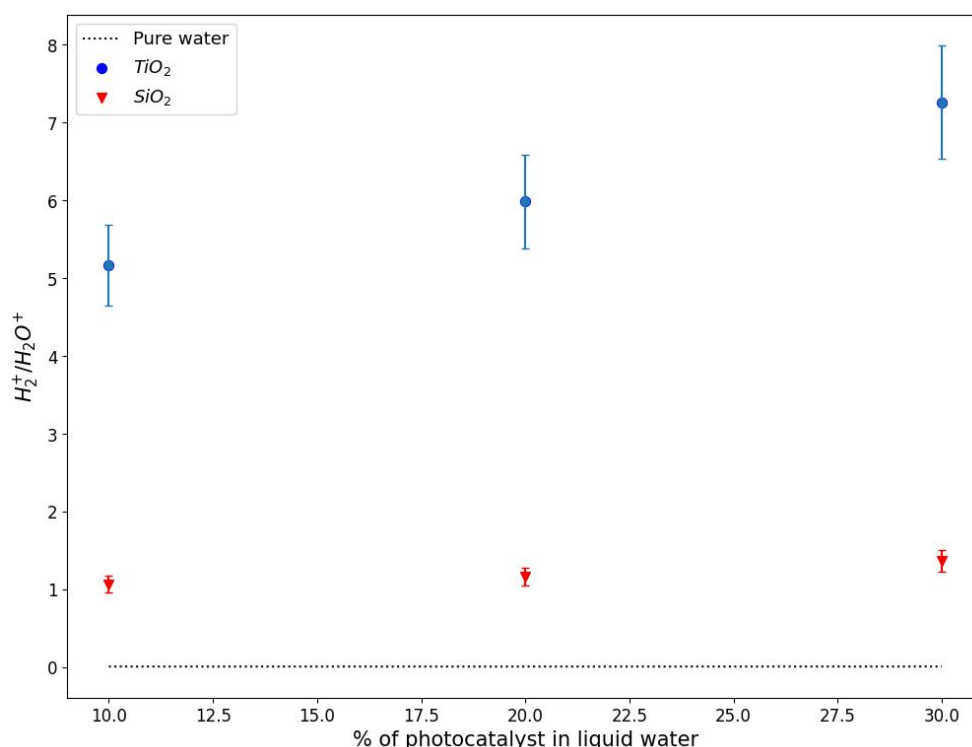


Figure 18 – The plot represents the ratio of H_2^+ / H_2O^+ for measurements using the TOF mass spectrometer involving varying percentages of photocatalyst in liquid water. The black dotted line represents measurements taken with pure water only, recorded over several irradiations on different days, serving as a basis for comparison. Data obtained with a photocatalyst present are represented by markers: the blue markers (circles) represent data for 10%, 20%, and 30% of TiO_2 ; the red markers (triangles) represent data for corresponding percentages of SiO_2 .

The plot presented provides a comparative analysis of hydrogen production under various experimental conditions. The black dotted line, representative of several measurements taken over different days using pure water, showcases a relatively consistent value for hydrogen production, indicative of stability in the absence of photocatalysts. The repeated data for pure water exhibited stability ($1.14 \times 10^{-2} \pm 3.00 \times 10^{-5}$). This consistency is visually demonstrated by the near-horizontal trend of this dotted line, which represents the mean of 1.14×10^{-2} , reinforcing the notion that the observed H_2 production reaches a constant value in such circumstances.

However, a markedly different scenario unfolds upon the introduction of photocatalysts. Both TiO_2 and SiO_2 , when introduced to the water, bring about an enhanced rate of

H_2 production. The data illustrates an enhancement in H_2 production that coincides with the increase in the proportion of photocatalyst present in the liquid water. This enhancement in production is represented by the upward trends marked by blue and red data points for TiO_2 and SiO_2 , respectively. The data points correspond to varying concentrations of the photocatalysts, specifically 10%, 20%, and 30%.

Of note is the relatively superior performance of TiO_2 as a photocatalyst. As depicted by the blue markers, the introduction of TiO_2 at all tested concentrations led to a higher yield of H_2 production when compared to both pure water and the SiO_2 -infused samples. This strongly suggests the potential of TiO_2 to act as an effective agent for increased hydrogen production in such setups.

On the other hand, CO_2 , present in air, could also be found in our measurements. When present in the system, carbon dioxide can interact with species produced by water radiolysis and alter the dynamics of the resulting chemical reactions.

In particular, e_{aq}^- , main precursor of H_2 in water radiolysis, can be scavenged by CO_2 , since the reaction between them would decrease the yield of H_2 . For this reason, we have additionally measured the system's CO_2^+ concentration, normalized by the concentration of H_2O^+ , as seen in Figure 19.

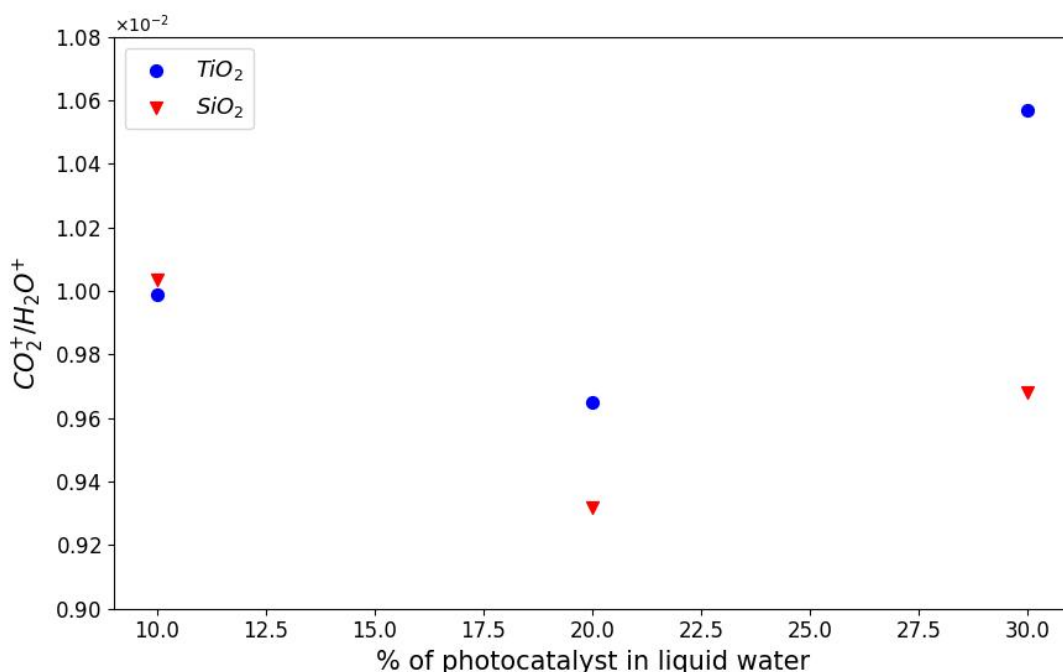


Figure 19 – The plot represents the ratio for measurements involving varying percentages of photocatalyst in liquid water, considering the amount of CO_2^+ normalized by the amount of H_2O^+ . Data obtained with the addition of photocatalysts are represented by markers: the blue markers (circles) represent data for 10%, 20%, and 30% of TiO_2 ; the red markers (triangles) indicate data for corresponding percentages of SiO_2 .

In all the conducted experiments, the concentration of CO_2 was observed to be quite low (on the order between 10^{-3} and 10^{-2}). Due to this minimal presence, its role can be largely seen as that of a contaminant within the experimental system. Hence, it's important to note that despite its presence, the impact of this CO_2 contamination on H_2 production appears to be negligible. The overarching results of the experiment, specifically pertaining to the production of H_2 [39], seem to remain substantially unaffected by this minor presence of CO_2 .

The data obtained for $\text{H}_2^+/\text{H}_2\text{O}^+$ ratios after the irradiations and the earlier-presented background measurement can then be compared, as shown in Table 4.

Measured ratios	H_2^+ / H_2O^+
Background measurement	0.0013
Pure water (avg)	0.0114
SiO_2 (15 g)	1.0669
SiO_2 (30 g)	1.1689
SiO_2 (45 g)	1.3690
TiO_2 (15 g)	5.1659
TiO_2 (30 g)	5.9876
TiO_2 (45 g)	7.2640

Table 4 – Comparison of the H_2^+ / H_2O^+ ratios, before and after irradiation, and with different proportions of photocatalysts.

Our experimental findings provide a confirmation of the Honda-Fujishima effect and shed light on the significant role of photocatalysts in the production of H_2 during water radiolysis. The observed enhancement in H_2 generation with the introduction of photocatalysts underscores their potential utility in the field of sustainable hydrogen production. These results contribute to a growing body of evidence supporting the mechanistic role of photocatalysts in the enhancement of radiolytic hydrogen production.

Chapter 5

Conclusions and future directions

Throughout the course of this study, our primary focus has been directed towards exploring the potential of the experimental apparatus in observing the products of water radiolysis, with a particular emphasis on the measurement of H_2 . Water radiolysis, a process with profound implications for a broad range of fields, presents a multitude of opportunities for detailed study. The ability to accurately measure the yield of H_2 , a product of radiolysis, represents a significant stride forward in the investigation of this process.

A comprehensive understanding of the capabilities of our experimental apparatus was integral to the achievement of our research objectives. The performance of the apparatus was assessed based on its ability to consistently yield accurate, reliable data. Special attention was paid to its proficiency in the measurement of H_2 , a key metric for evaluating the success of water radiolysis.

Upon careful evaluation of the results, it is possible to conclude that both the experimental apparatus and the methodology employed have proven to be well-suited for the task at hand. The apparatus demonstrated a commendable level of performance, effectively capturing the essential aspects of water radiolysis and accurately measuring H_2 yields. The methodology, characterized by its systematic approach and rigorous procedures, provided the necessary framework to guide our investigation.

In conclusion, our study confirms the adequacy of both the experimental apparatus

and the methodology used for the measurement of H_2 yields in the context of water radiolysis. It is our belief that these future findings can serve as a solid foundation for future investigations in this domain, contributing to the growing body of knowledge on water radiolysis and its various applications.

Future research efforts may build upon these findings, further refining the experimental apparatus and methodology, and extending the investigation to explore other aspects of water radiolysis. As we continue to delve into the complexities of this fascinating process, each discovery propels us forward, bringing us one step closer to fully unlocking the potential of water radiolysis.

As we look towards the future, several promising avenues for further research are apparent. One of these involves the variation of different parameters within the experimental process. Factors such as temperature and magnetic field intensity, which according to the existing literature [40] are anticipated to influence the yield of H_2 , are prime candidates for exploration. By modulating these variables, we can gain deeper insights into their impact on the process of water radiolysis and potentially unlock new ways of optimizing H_2 production.

In addition to these parameters, we also recommend the investigation of different types and combinations of photocatalysts. Our current findings have demonstrated the significant role of photocatalysts in enhancing H_2 production during water radiolysis. Further exploration of this avenue could lead to even more effective and efficient ways of generating H_2 , aiding in the optimization of this process.

In conclusion, the field of water radiolysis, especially when paired with photocatalysis, has a significant role to play in the pursuit of sustainable energy solutions. The production of 'green' hydrogen via water radiolysis stands as a promising alternative to traditional, non-renewable sources of energy. It offers the prospect of a clean, abundant, and efficient energy source, aiding in our collective goal of reducing greenhouse gas emissions and mitigating the impacts of climate change.

As our society continues to grapple with the implications of our energy choices, studies like this one underscore the immense potential that lies within alternative, renewable sources of energy. With continued exploration, optimization, and innovation in the field of water radiolysis, we move ever closer to harnessing the full potential of green hydrogen as a cornerstone of a sustainable energy future.

References

- 1 DRAGANIC, I.; DRAGANIC, Z. *The Radiation Chemistry of Water*. [S.l.]: Academic Press, 1971.
- 2 PIRRONELO, V. et al. Formation of molecular hydrogen: The mother of all molecules. In: *Exobiology: Matter, Energy, and Information in the Origin and Evolution of Life in the Universe*. [S.l.]: Springer Netherlands, 1998.
- 3 GREENWOOD, N.; EARNSHAW, A. *Chemistry of the elements*. [S.l.]: Butterworth-Heinemann, 1997.
- 4 SIGAUD, L.; MONTENEGRO, E. Total neutral H_2 and H production from ethylene by electron-impact ionization. *Phys. Rev. A*, v. 102, 2020.
- 5 HOFFMANN, P. *Tomorrow's Energy Hydrogen, Fuel Cells, and the Prospects for a Cleaner Planet*. [S.l.]: The MIT Press, 2001.
- 6 ALI, I. et al. Role of the radiations in water splitting for hydrogen generation. *Sustainable Energy Technologies and Assessments*, v. 51, 2022.
- 7 LE CAËR, S. Water radiolysis: Influence of oxide surfaces on H_2 production under ionizing radiation.
- 8 KREIPL, M.; FRIEDLAND, W.; PARETZKE, H. Time- and space-resolved Monte Carlo study of water radiolysis for photon, electron and ion irradiation. *Radiat Environ Biophys*, v. 48, p. 11–20, 2009.
- 9 LAVERNE, J. Radiation chemical effects of heavy ions. in: Mozumder, A. and Hatano, Y., Charged particle and photon interactions with matter: Chemical, physicochemical, and biological consequences with applications. Marcel Dekker, p. 403–429, 2004.
- 10 PASTINA, B.; LAVERNE, J.; PIMBLOTT, M. Dependence of molecular hydrogen formation in water on scavengers of the precursor to the hydrated electron. *J. Phys. Chem. A*, v. 103, p. 5841–5846, 1999.
- 11 DEL GIUDICE, E. *et al.* Coherent structures in liquid water close to hydrophilic surfaces. *J. Phys.: Conf. Ser.*, v. 442, 2013.
- 12 BASSANI, F. et al. *Encyclopedia of Condensed Matter Physics*. [S.l.]: Academic Press, 2005.

- 13 FIEDLER, J. et al. Full-spectrum high-resolution modeling of the dielectric function of water. *Journal of Physical Chemistry B*, v. 124, p. 3103–3113, 2020.
- 14 BRODSKY, A. B. *Handbook of Radiation Measurement and Protection*. [S.l.]: CRC Press, 1978.
- 15 L. R. Castillo-Rico et al. Stopping power and CSDA range of electrons in liquid water, LiF , CaF_2 , and Al_2O_3 from the energy gap up to 433 keV. *Nuclear Inst. and Methods in Physics Research, B*, v. 502, p. 189–197, 2021.
- 16 MONTENEGRO, E. et al. Evaporation, fission and auto-dissociation of doubly charged water. *Journal of electron spectroscopy and related phenomena*, v. 155, p. 81–85, 2007.
- 17 COBUT, V. et al. Monte Carlo simulation of fast electron and proton tracks in liquid water. I. Physical and physicochemical aspects. *Radiat. Phys. Chem.*, v. 51, p. 229–243, 1998.
- 18 UEHARA, S.; NIKJOO, H. Monte Carlo simulation of water radiolysis for low-energy charged particles. *J. Radiat. Res.*, v. 47, p. 69–81, 2006.
- 19 FRONGILLO, Y. et al. Monte Carlo simulation of fast electron and proton tracks in liquid water. II. Nonhomogeneous chemistry. *Radiat. Phys. Chem.*, v. 51, p. 245–254, 1998.
- 20 PASTINA, B.; LAVERNE, J. Effect of molecular hydrogen on hydrogen peroxide in water radiolysis. *J. Phys. Chem. A*, v. 105, p. 9316–9322, 2001.
- 21 SPINKS, J.; WOODS, R. *An introduction to radiation chemistry*. [S.l.]: John Wiley Sons, Inc., 1990.
- 22 LUNA, H.; MONTENEGRO, E. Fragmentation of water by heavy ions. *PRL*, v. 94, 2005.
- 23 LUNA, H. et al. Water-molecule dissociation by proton and hydrogen impact. *Physical Review A*, v. 75, 2007.
- 24 FERREIRA, Natalia; SIGAUD, L.; MONTENEGRO, E. Three-body fragmentation from single ionization of water by electron impact: The role of satellite states. *JPCA*, v. 121, p. 3234–3238, 2017.
- 25 FERREIRA, Natalia; SIGAUD, L.; MONTENEGRO, E. Kinetic energy distribution of OH^+ from water fragmentation by electron impact. *Phys. Rev. A*, v. 96, 2017.
- 26 HERBERT, J.; COONS, M. The hydrated electron. *Annu. Rev. Phys. Chem.*, v. 68, 2017.
- 27 POLITZER, P.; ABU-AWWAD, F. A comparative analysis of hartree-fock and kohn-sham orbital energies. *Theoretical Chemistry Accounts*, v. 99, p. 83–87, 1998.
- 28 LUDWIG, V.; COUTINHO, K.; CANUTO, S. Sequential classical-quantum description of the absorption spectrum of the hydrated electron. *Physical Review B*, v. 70, 2004.
- 29 LAVERNE, J. A.; PIMBLOTT, S. New mechanism for H_2 formation in water. *J. Phys. Chem. A*, v. 104, p. 9820–9822, 2000.
- 30 FUJISHIMA, A.; HONDA, K. Electrochemical photolysis of water at a semiconductor electrode. *Nature*, v. 238, p. 37–38, 1972.

- 31 ABE, R. Recent progress on photocatalytic and photoelectrochemical water splitting under visible light irradiation. *Journal of Photochemistry and Photobiology C: Photochemistry Reviews*, v. 11, p. 179–209, 2010.
- 32 KUDO, A.; MISEKI, Y. Heterogenous photocatalyst materials for water splitting. *Chemical Society Reviews*, v. 38, 2009.
- 33 LAVERNE, J. A.; TONNIES, S. E. H_2 production in the radiolysis of aqueous SiO_2 suspensions and slurries. *J. Phys. Chem. B*, v. 107, p. 7277–7280, 2003.
- 34 DAMBOURNET, D. et al. Tailored preparation methods of TiO_2 anatase, rutile, brookite: Mechanism of formation and electrochemical properties. *Chem. Mater.*, v. 22, 2010.
- 35 H. M. Moura, M. M. Unterlass. Biogenic metal oxides. *Biomimetics*, v. 5, 2020.
- 36 SIGAUD, L. et al. A novel double-focusing time-of-flight mass spectrometer for absolute recoil ion cross sections measurements. *Rev. Sci. Instrum.*, v. 87, 2016.
- 37 SIGAUD, L. et al. Cross-section measurements for the fragmentation of $CHClF_2$ by electron impact. *J. Phys. B: At. Mol. Opt. Phys.*, v. 43, 2010.
- 38 MCGRADY, J. et al. H_2 generation at metal oxide particle surfaces under γ -radiation in water. *Journal of Nuclear Science and Technology*, 2020.
- 39 LEAL, M. *Determinação da energia cinética do íon H_3^+ resultante de reações secundárias utilizando a técnica DETOF*. Dissertação (Mestrado) — Universidade Federal Fluminense, 2020.
- 40 DUENAS, J. et al. Effect of low intensity static magnetic field on purified water in stationary condition: Ultraviolet absorbance and contact angle experimental studies. *Journal of Applied Physics*, v. 127, 2020.
- 41 ZUMDAHL, S.; ZUMDAHL, S. *Chemistry*. [S.l.]: Cengage Learning, 2013.
- 42 CHAPLIN, M. *Water molecule structure*. 2020. <http://https://water.lsbu.ac.uk/water/water_molecule.html>. Accessed June/2023.
- 43 CHAPLIN, M. *Molecular Orbitals for Water*. 2001. <http://https://water.lsbu.ac.uk/water/h2o_orbitals.html>. Accessed June/2023.
- 44 BAIBICH, I.; BUTLER, I. A brief introduction to molecular orbital theory. *Quim. Nova*, v. 35, 2012.
- 45 MACHADO, S.; FARIA, R. Explaining the geometry of simple molecules using molecular orbital energy-level diagrams built by using symmetry principles. *Quim. Nova*, v. 41, 2018.
- 46 CHAPLIN, M. *Hydrogen bonding in water*. 2000. <http://https://water.lsbu.ac.uk/water/water_hydrogen_bonding.html>. Accessed June/2023.
- 47 JOSHI, A. W. *Elements of group theory for physicists*. [S.l.]: New Age International, 1997.
- 48 DRESSELHAUS, M. S. et al. *Group Theory: Application to the Physics of Condensed Matter*. [S.l.]: Springer-Verlag, 2008.

Appendix A

Water molecule

A.1 Molecular structure

Water is a molecule composed of two hydrogen atoms and one oxygen atom, with four pairs of electrons: two bonding pairs and two non-bonding pairs, which, in order to minimize repulsion, are distributed in a tetrahedral arrangement. Although these electron pairs are distributed in a tetrahedral shape, the water molecule takes on a V shape, with oxygen at the vertex and one hydrogen at each end, forming a curvature angle of 104.5 degrees in the gaseous state and 105.5 degrees in the liquid state; the angle is larger in liquid water due to hydrogen bonding. This shape is a consequence of the presence of non-bonding electron pairs, also known as lone pairs, as these pairs are closer to the oxygen atom than the bonding pairs are to the hydrogen atoms and therefore require more space. There is greater repulsion between the non-bonding pairs, which forces the bonds $O-H$ to remain even more cohesive, compressing the angle between the bonding pairs.

A physical interpretation of the bonding and non-bonding electron pairs is that a bonding pair is shared between two nuclei, allowing the electrons to be close to each of these nuclei and relatively confined between them. On the other hand, a non-bonding pair is restricted to a single nucleus, resulting in its electrons being close to that nucleus. Without these non-bonding pairs, the water molecule would be linear, and there would be no electric dipole moment. This dipole moment arises from the fact that the electron wave function is

more dense around the oxygen atom compared to the hydrogen atoms. As a result, there is a concentration of positive charges around the hydrogen atoms and negative charges around the oxygen, leading to a polar molecule, an important property of water [41].

The figure 20 depicts the charge distribution and electronic density of a water molecule. The charge distribution of an isolated molecule is significantly influenced by the molecular geometry and the method used for calculation, but it typically results in approximately $-0.7e$ for the oxygen atom, and an equal but opposite charge distribution shared between the hydrogen atoms [42].

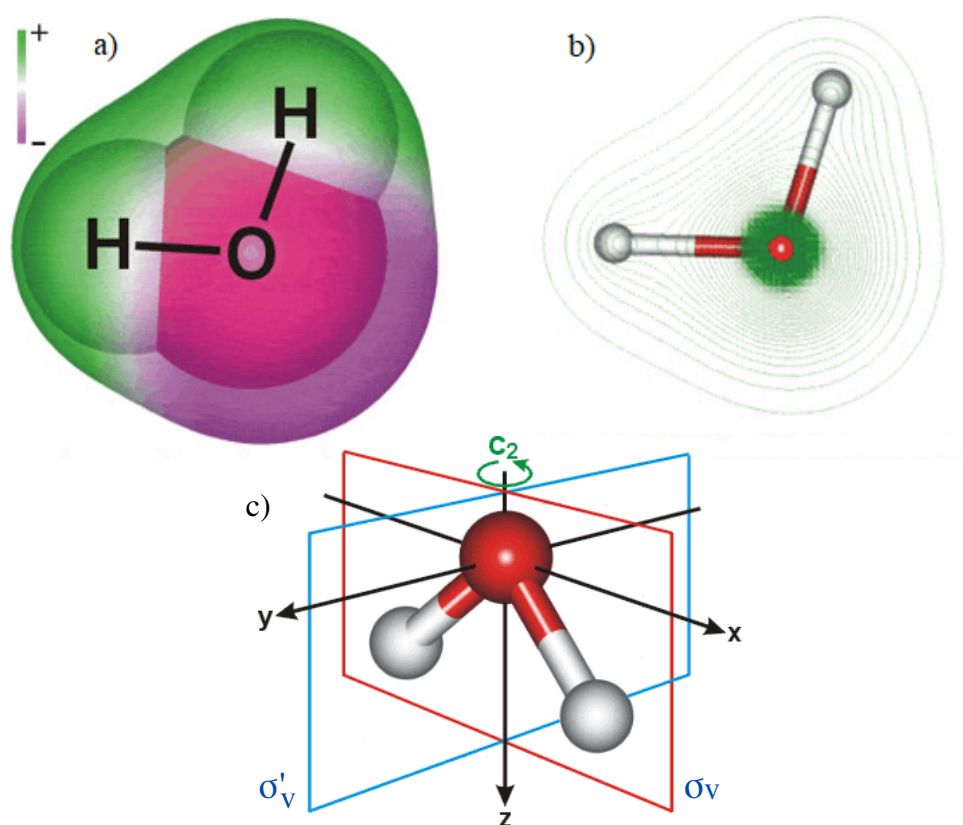


Figure 20 – a) The approximate shape and charge distribution of the water molecule. b) Electronic density of the water molecule. c) Symmetry axes of the water molecule, with C_2 as the principal axis, and σ_v and σ'_v as the mirror planes. Figure taken from [42].

The unequal distribution of electronic density illustrated above is responsible for the polarity of the water molecule. An electrostatic attraction between the partially positive charge around the H atoms and the partially negative charge around the O atom results in

the formation of hydrogen bonds. These hydrogen bonds, in turn, give rise to other important properties of water, such as the solubility of ions and other molecules, strong surface tension, and high specific heat capacity [42].

A.2 Molecular orbitals

The water molecule exhibits a specific angle of curvature, making it a non-linear molecule. It belongs to the C_{2v} symmetry group (see Appendix B), possessing symmetry around its principal axis under a rotation of π , as well as reflection symmetry with respect to the xz and yz planes. Table 5 displays the characters of the C_{2v} group, which are essential for constructing the molecular orbitals of water.

The notation of molecular orbitals in water derives from the C_{2v} symmetry group. Each atomic orbital exhibits symmetry around the principal axis and mirror axes. The overlap of atomic orbitals between oxygen and hydrogen will occur between orbitals with the same symmetry. As a result, the molecular orbitals formed possess symmetry and are labeled according to the conventions of the C_{2v} group.

C_{2v}	E	C_2	$\sigma_v(xz)$	$\sigma'_v(yz)$	Base
a_1	1	1	1	1	z
a_2	1	1	-1	-1	
b_1	1	-1	1	-1	x
b_2	1	-1	-1	1	y

Table 5 – Character table of the C_{2v} group.

The table above displays the symmetry operations of the C_{2v} group, starting with the operation E, which is the identity symmetry operation. The C_2 operation represents a rotation of π around the principal axis, i.e., the z-axis containing the central atom. The σ_v and σ'_v operations represent rotations around the xz and yz mirror planes, respectively. The orbitals a and b are associated with the sign of the wave function after rotation along the principal axis. If the wave function retains the same sign, it corresponds to an orbital a ; otherwise, it corresponds to an orbital b . On the other hand, the subscripted numbers 1 and 2

are linked to reflection in the xz plane. If the sign of the wave function remains unchanged, the orbital is labeled with the subscript 1, and if there is a change in the sign of the wave function, the orbital is labeled with the subscript 2. Finally, the table also shows the sign of the wave function after each symmetry operation, with 1 indicating no change in sign and -1 indicating a change in sign [43].

Once the character table and their relationships are known, the next step is to construct the molecular orbitals based on the symmetry of the atomic orbitals. Therefore, the first task is to determine the symmetries of the valence orbitals of the central atom, which in this case is oxygen. Oxygen has eight electrons distributed among five orbitals: $1s$, $2s$, $2p_x$, $2p_y$, and $2p_z$. Six electrons are located in the two valence shells, $2s$ and $2p_{xyz}$. The symmetries of these shells can be directly obtained from Table 5. By assumption, the $2s$ orbital belongs to the a_1 orbital since all s orbitals possess spherical geometry and, therefore, have total symmetry. On the other hand, the symmetries of the $2p_x$, $2p_y$, and $2p_z$ orbitals are also determined from the table, corresponding to b_1 , b_2 , and a_1 , respectively [44].

Each hydrogen atom has a $1s$ orbital. It is necessary to generate a reducible representation Γ , which represents the changes that occur when each symmetry operation is applied. For each $1s$ orbital, a value of 1 should be assigned if the orbital remains in the same position after the operation, or 0 if the orbital is moved from its original position [45]. Therefore, the following reducible representation is obtained, according to Table 6:

C_{2v}	E	C_2	$\sigma_v(xz)$	$\sigma'_v(yz)$
Γ_{1s}	2	0	0	2

Table 6 – Reducible representation Γ .

Next, it is possible to reduce this Γ representation into irreducible representations within the C_{2v} symmetry group. In this case, the irreducible representations are the a_1 and b_2 orbitals, which indeed represent the symmetries for the two hydrogen atoms. Table 7 demonstrates that the combination of the a_1 and b_2 orbitals yields the Gamma representation.

C_{2v}	E	C_2	$\sigma_v(xz)$	$\sigma'_v(yz)$
Γ_{1s}	2	0	0	2
a_1	1	1	1	1
b_2	1	-1	-1	1

Table 7 – Irreducible representations of Γ and H atoms symmetries.

The superposition of atomic orbitals with the same symmetry is responsible for the formation of molecular orbitals. Therefore, the a_1 orbital of the two hydrogen atoms overlaps with the two a_1 orbitals related to the $2s$ and $2p_z$ shells of the oxygen atom, generating two molecular orbitals with a_1 symmetry. Similarly, the b_2 orbital of the two hydrogen atoms overlaps with the b_2 orbital related to the $2p_y$ shell of the oxygen atom, forming a molecular orbital with b_2 symmetry. On the other hand, the b_1 orbital of the $2p_x$ shell of the oxygen atom does not have symmetry with any orbital of the hydrogen atoms and, therefore, does not contribute to the molecular bonding. This b_1 orbital has a lone pair of electrons, which is responsible for the hydrogen bonding between the molecules, which will be described next [44]. Figure 21 illustrates these orbitals of the H_2O molecule with their respective energies, including the anti-bonding orbitals.

In this figure, the orbitals are numbered from lowest to highest energy using the notation $1a_1$, $2a_1$, $3a_1$, and so on. Additionally, Figure 21 illustrates the shapes of the molecular orbitals, with color differentiation representing the signs of the wave function.

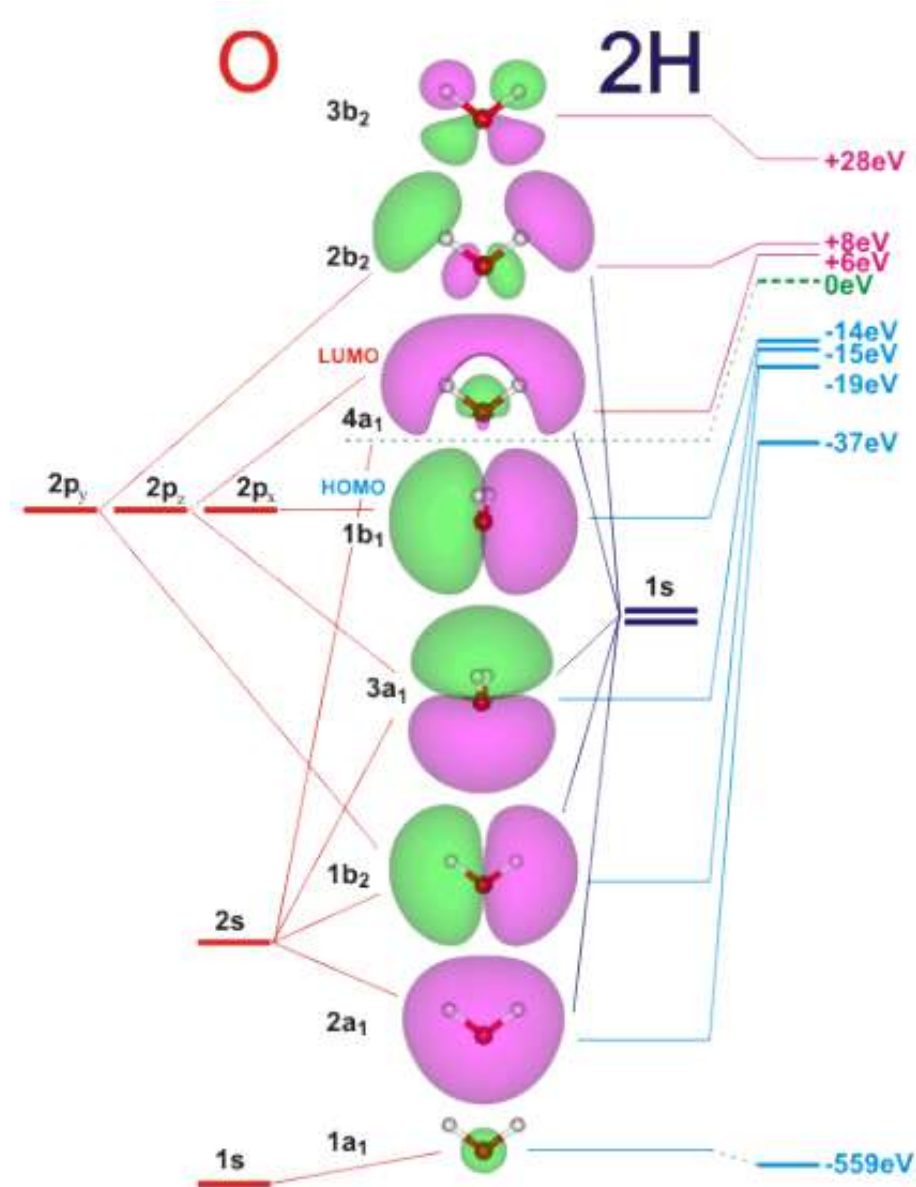


Figure 21 – Bonding and anti-bonding orbitals of the H_2O molecule. HOMO represents the highest occupied molecular orbital, while LUMO is the lowest unoccupied molecular orbital. Figure taken from [43].

A.3 Hydrogen bonding

The highest occupied molecular orbital, also known as the $1b_1$ orbital as shown in Figure 21, does not participate in the covalent bonding process responsible for the formation of the water molecule. Therefore, this orbital, belonging to the $2p_x$ subshell of the oxygen

atom, is associated with anti-bonding electron pairs, which are closer to the oxygen atom and responsible for the negative charge density around oxygen and, consequently, for the polarity and geometry of the H_2O molecule.

The negative charge density attracts hydrogen atoms from other molecules, giving rise to new bonds known as hydrogen bonds. Although, these hydrogen bonds are considerably weaker than covalent bonds, having a strength equivalent to only 5% of a covalent bond. Remarkably, each H_2O molecule can form connections with four others through hydrogen bonding, due to an enthalpic process that maximizes the number and strength of these hydrogen bonds. These bonds are constantly breaking, occurring trillions of times per second. However, thanks to the cooperative nature of the system, when a breakage occurs, the system tends to reorganize itself by forming new bonds. The formation of these bonds happens randomly, resulting in a tetrahedral structure for the linked molecules.

Due to the constant breaking and reforming of hydrogen bonds among water molecules in its liquid state, these bonds are responsible for imparting significant properties to the water molecule, such as its high thermal capacity. When heat is absorbed, a portion of it primarily contributes to breaking the hydrogen bonds. Only after the hydrogen bonds are broken can water molecules move freely, resulting in reduced temperature variation. This is because temperature is directly related to the average kinetic energy of the molecules. As a result, hydrogen bonds play a crucial role in conferring water's important property of high thermal capacity [46].

Appendix B

Group theory

B.1 What is a Group?

A group, in general, consists of a set of elements combined with a binary operation rule between each of these elements, which varies according to the specific group being considered. Additionally, there are four inherent axioms in all structured sets of the aforementioned form: identity, closure, associativity, and existence of inverse elements. One can formally define a group as follows:

Definição 1 *Groups (formal)*

A group G is a set of elements a, b, c, \dots with a multiplication rule, satisfying the following conditions:*

- *Identity: $\forall a \in G, \exists \text{ an element } E \text{ such that } a.E = E.a = a$;*
- *Closure: $a, b \in G \longrightarrow a.b = c \in G$;*
- *Associativity: $a, b, c \in G \longrightarrow a.(b.c) = (a.b).c$;*
- *Inverse: $\forall a \in G, \exists \text{ an } a^{-1} \text{ such that } a.a^{-1} = a^{-1}.a = E$.*

*In the context of Group Theory, multiplication refers to any rule of association between two elements of the group, resulting in a third element that also belongs to the group.

There are infinite ways to construct sets whose elements satisfy Definition 1. Some examples of groups are:

1. All real numbers under “+”;
2. All real numbers, except zero, under “×”;
3. All rotations in a three-dimensional space: $O(3)$;
4. All $n \times n$ matrices, real and invertible, under “×”: $GL(n, \mathbb{R})$ (*General Linear Group*);
5. All $n \times n$ orthogonal matrices with determinant 1, under “×”: $SO(n)$ (*Special Orthogonal Group*);
6. All unitary matrices with determinant 1, under “×”: $SU(n)$ (*Special Unitary Group*).

An example of a set that does not form a group would be the set of integers under multiplication, in which it can be easily verified that there is no inverse element.

B.2 Classification of groups

In the examples of groups presented in the previous section, it can be noted that the objects forming a group are diverse, ranging from numbers with simple algebraic operations to three-dimensional rotations. In particular, the latter is known as a continuous group, while the former is classified as a discrete group. However, there are some intermediate definitions to be established preliminarily in order to ensure a good understanding of these classifications.

Definição 2 *Order of a group*

The order of a group G , denoted by $|G|$, is the number of elements in G .

The order of a given group should not be confused with the order of an element of the group.

Definição 3 *Order of an element*

Let g be an element of a group G . The order of g is defined as the number of times g must be "multiplied" by itself until the identity element of G is obtained.

Thus, a group can be classified as finite or infinite, using the appropriate language of Group Theory:

Definição 4 *Finite and infinite groups*

A group G is said to be finite if its order is finite. Conversely, the group is infinite if its order is infinite.

Example: $(GL(2, \mathbb{R}), \times)$

Clearly, this is a group of infinite order, as it includes all matrices with nonzero determinants and real entries. However, its elements can have finite order. In fact, consider a matrix $M \in GL(2, \mathbb{R})$ such that:

$$M = \begin{pmatrix} \frac{\sqrt{3}}{2} & \frac{-1}{2} \\ \frac{1}{2} & \frac{\sqrt{3}}{2} \end{pmatrix}. \quad (\text{B.1})$$

This element has an order of 12 ($|M| = 12$), which means that

$$M^{12} = \begin{pmatrix} 1 & 0 \\ 0 & 1 \end{pmatrix}. \quad (\text{B.2})$$

Therefore, the order of a group and the order of its elements are distinct definitions.

Lastly, groups can be classified as discrete or continuous. Essentially, a definition of continuous groups is sufficient, and by exclusion, it is possible to determine whether a group is discrete or not.

Definição 5 *Continuous Groups*

A group G is said to be continuous if its elements are functions of real parameters $\alpha_1, \alpha_2, \dots, \alpha_n$, where one or more of these parameters vary continuously within a certain interval. Moreover, these parameters must be sufficient and necessary to characterize all the elements of the group.

A simple example of a continuous group is $SO(2)$, whose elements represent rotations in a two-dimensional space. In fact, it is common to represent this group using 2×2 orthogonal matrices, whose entries are functions of a parameter θ that varies continuously within an interval from 0 to 2π .

B.3 Group Representation

In this section, the theory of group representation will be addressed. The idea is to represent the elements of a given group using non-singular square matrices.

Definição 6 *Representation of Discrete Groups*

Let $G = \{A_i; i = 1, \dots, n\}$ and $T = \{T(A_i); i = 1, \dots, n\}$ be two finite groups, where T is a group of non-singular $n \times n$ matrices. T is said to be a representation of $G \iff \forall A_i \in G \exists a T(A_i) \in T$ such that:

$$T(A_i)T(A_j) = T(A_i A_j). \quad (\text{B.3})$$

In this case, T is an order- n representation of the group G .

In Quantum Mechanics, there is often an interest in unitary operators, as they preserve inner product and, consequently, probabilities. Therefore, it is desirable to search for a representation T of a given group of interest that is unitary. In fact, through a change of basis,

it is possible to change the matrix representation of an operator. Mathematically, given a $T(A_i) \in T$, there will always exist a unitary representation $\Gamma(A_i) \in \Gamma$ such that:

$$\Gamma(A_i) = V^{-1} T(A_i) V \quad (\text{B.4})$$

Equation B.4 represents a similarity transformation, which demonstrates how an operator varies under a change of basis.

Unitary representations, besides being relevant in Quantum Mechanics, are associated with a fundamental theorem of representation theory. Before presenting the theorem, the following definition should be considered:

Definição 7 *Completely reducible representation*

Given a finite group G , a completely reducible representation T is one in which the matrices can be put into block-diagonal form.

Now, the theorem will make more sense:

Teorema 1 *Unitary representations are completely reducible.*

Combining the theorem with definition 7, it follows that the unitary matrix representations of a group are of the form:

$$\Gamma(A_i) = \left[\begin{array}{c|c} \Gamma^{(1)}(A_i) & 0 \\ \hline 0 & \Gamma^{(2)}(A_i) \end{array} \right]. \quad (\text{B.5})$$

This means that instead of considering matrices that represent G in the entire vector space L_n of dimension n , one can search for representations within subspaces of L_n . When this is possible, it is said that the subspaces are invariant[†] under the action of G .

[†]Invariance means that the elements of G act on objects in the space and map back to the space, forming a closed operation.

$\Gamma^{(1)}(A_i)$ is a set of representations of the elements $A_i \in G$ in an invariant subspace of L_n , while $\Gamma^{(2)}(A_i)$ refers to another invariant subspace. The matrix in B.5 is just an example used for simplicity, but it could be formed by more diagonal blocks, as long as there are more invariant subspaces. Thus, in general, a completely reducible representation can be expressed as

$$\Gamma(A_i) = \bigoplus_{j=1}^n c_j \Gamma^{(j)}(A_i), \quad (\text{B.6})$$

where each $\Gamma^{(j)}$ corresponds to a representation in a minimal invariant subspace of G , meaning that it cannot be further subdivided into any other invariant subspace. That is why the $\Gamma^{(j)}$'s are called irreducible representations.

It is worth noting that non-unitary representations can also be completely reducible, except that in this case, there is no theorem guaranteeing that it will always be possible. A good example is the rotations in \mathbb{R}^3 , which form the group $\text{SO}(3)$. Considering a passive rotation around the z -axis, where the rotation angle increases positively in the counterclockwise direction, the elements of $\text{SO}(3)$ can be represented by

$$R(\theta) = \left[\begin{array}{cc|c} \cos \theta & \sin \theta & 0 \\ -\sin \theta & \cos \theta & 0 \\ \hline 0 & 0 & 1 \end{array} \right]. \quad (\text{B.7})$$

The first block corresponds to the xy plane, while the second block is one-dimensional and corresponds to the space formed by the points on the z -axis. It is easy to see that both are subspaces of \mathbb{R}^3 that are invariant under the specified rotations. It is also observed that the matrix structure is in the form of a direct sum, as defined in B.6, and the irreducible representation

$$\left[\begin{array}{cc} \cos \theta & \sin \theta \\ -\sin \theta & \cos \theta \end{array} \right], \quad (\text{B.8})$$

is a faithful representation of the elements of $\text{SO}(2)$ (the group of rotations in the plane).

B.4 Transformation Groups

In section B.2, it was seen that groups can be classified in various distinct ways. It was also mentioned in section B.1 that there are groups of different natures. This time, the focus will be on a description of groups whose elements represent transformations[‡].

A physical theory is usually described by a set of equations of motion for the relevant dynamic variables of a given system. The solutions to these equations should represent physical realities; for example, the fields \vec{E} and \vec{B} are the dynamic variables for the Maxwell's equations, which predict the existence of electromagnetic waves (physical reality). It is common for a physical system to exhibit certain symmetries, from which one can take advantage to describe some properties of the system. Essentially, a symmetry in physics can be thought of as a transformation that leaves the relevant equations of motion invariant, or even a transformation between equivalent reference frames.

Therefore, in physics, the groups of interest are those whose elements represent transformations (rotations, translations, reflections, etc.) on a given system. Furthermore, the interest lies in the so-called symmetry groups, which, as mentioned above, are transformation groups that leave the physical system invariant. Generally, a symmetry in physics is directly related to transformations of reference frames, and it can be said that they are transformations with geometric significance. This significance is very useful for qualitatively seeking symmetries, that is, one can consider transformations on the coordinates and investigate whether these transformations leave the system invariant without having to go through the equations of motion. In the model of an infinite homogeneous plate with surface charge density σ , for example, it is easy to see, through these arguments, that there will be translation symmetry. This means that an observer A, located at the origin of a Cartesian coordinate system, will perceive the same physical properties in space (charge distribution) as a second observer B, whose coordinate system is simply the origin of A translated, as shown in figure 22. Therefore, note how it was possible, with the aid of a reference frame, to analyze the

[‡]For the water molecule, the main interest will be in rotational transformations.

problem geometrically without the need to verify whether the translated Maxwell's equations are invariant.

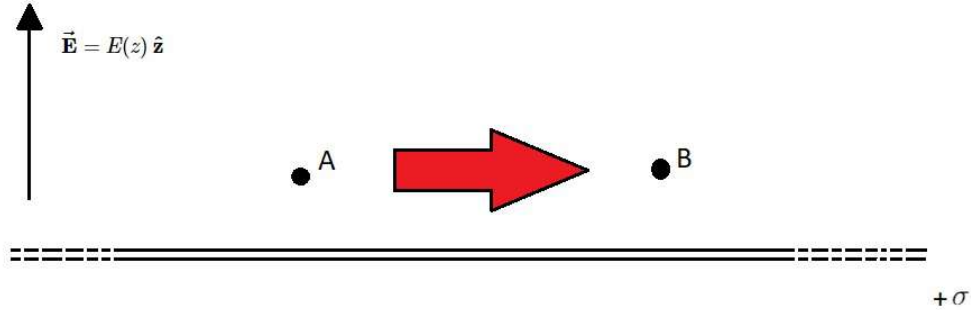


Figure 22 – Translation symmetry in an infinite plane with a positive charge density.

It is easy to convince oneself that the set of all symmetry operations of a physical system forms a group structure. Firstly, note that two symmetry operations, when applied successively to the system, must, by definition of these operations, leave it invariant. Therefore, this successive application should generate a third symmetry operation of the system, indicating closure of the group. The identity element corresponds to not performing any operation on the system, making it the most trivial symmetry operation that can be executed. It is also possible to reverse such operations, leading to the existence of inverse elements. Finally, the successive application of symmetries should be associative.

Example: Consider the symmetry group of an equilateral triangle (D_3). The operations are:

- Identity (E): No transformation is applied.
- Rotation (C_3): The triangle is rotated counterclockwise by $\frac{2\pi}{3}$ radians (or 120°).
- Rotation (C_2): The triangle is rotated counterclockwise by π radians (or 180°).
- Rotation (C_1): No rotation is applied.
- Reflection (σ_1): Reflection across one of the three axes of symmetry.

- Reflection (σ_2): Reflection across a different axis of symmetry.
- Reflection (σ_3): Reflection across the remaining axis of symmetry.

These operations form the symmetry group D_3 , which describes all the possible symmetries of an equilateral triangle.

Note that, for example, if a 360° rotation is performed on the triangle in the plane that contains it, it corresponds to multiplying the elements AB of the group, such that $AB=E$. The multiplication rule, strictly speaking, can be established as a composition of functions.

We could think about this same problem in a more interesting way for Physics, such as transformations on coordinates. It is well-known that many groups of interest in Physics are geometric in nature, so it is possible to think of their elements as transformations on coordinate systems. As an example, establish a Cartesian coordinate system on the equilateral triangle and consider a passive rotation of 120° , i.e., a rotation of the coordinate axes themselves while the triangle remains fixed (as shown in Figure 23). Thus, we can represent the element A using a matrix equation:

$$\vec{x}' = T(A)\vec{x}, \quad (\text{B.9})$$

or explicitly:

$$\begin{pmatrix} x' \\ y' \end{pmatrix} = \begin{pmatrix} -\frac{1}{2} & \sqrt{\frac{3}{2}} \\ -\sqrt{\frac{3}{2}} & -\frac{1}{2} \end{pmatrix} \begin{pmatrix} x \\ y \end{pmatrix}. \quad (\text{B.10})$$

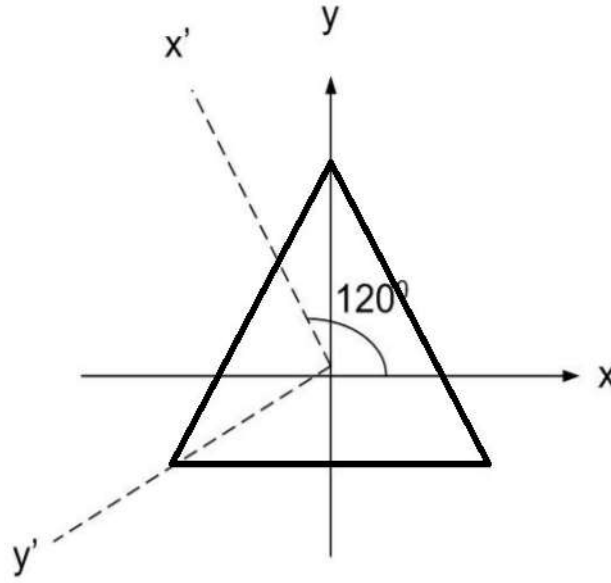


Figure 23 – Equilateral triangle under passive rotation.

The remaining elements of D_3 can be obtained in a similar manner:

$$T(B) = \begin{pmatrix} -\frac{1}{2} & -\sqrt{\frac{3}{2}} \\ \sqrt{\frac{3}{2}} & -\frac{1}{2} \end{pmatrix}, \quad T(E) = \begin{pmatrix} 1 & 0 \\ 0 & 1 \end{pmatrix}, \quad T(K) = \begin{pmatrix} -1 & 0 \\ 0 & 1 \end{pmatrix},$$

$$T(L) = \begin{pmatrix} \frac{1}{2} & -\sqrt{\frac{3}{2}} \\ -\sqrt{\frac{3}{2}} & -\frac{1}{2} \end{pmatrix}, \quad T(M) = \begin{pmatrix} \frac{1}{2} & \sqrt{\frac{3}{2}} \\ \sqrt{\frac{3}{2}} & \frac{1}{2} \end{pmatrix}.$$

Note that we used a representation vector space, in this case \mathbb{R}^2 , to obtain the matrix representations for the elements of D_3 [47].

B.5 Characters of a representation

Definição 8 Characters

The character of the representation matrix $\chi^{(\Gamma_j)}(R)$ for a symmetry operation R in a representation $D^{(\Gamma_j)}(R)$ is the trace (or the sum over all elements of the diagonal) of the matrix representation:

$$\chi^{(\Gamma_j)}(R) = \text{Tr} D^{(\Gamma_j)}(R) = \sum_{\mu=1}^{\ell_j} D^{(\Gamma_j)}(R)_{\mu\mu}, \quad (\text{B.11})$$

where ℓ_j is the dimensionality of the representation Γ_j and j is an index of the representation. From the definition, it follows that the representation Γ_j will have h characters, one for each element of the group. Since the trace of a matrix is invariant under a similarity transformation, the character is also invariant under such transformation [48].